Published in final edited form as:

J Phys Chem B. 2017 April 27; 121(16): 4023–4039. doi:10.1021/acs.jpcb.7b02320.

Building a More Predictive Protein Force Field: A Systematic and Reproducible Route to AMBER-FB15

Lee-Ping Wang[1], **Keri A McKiernan**[2], **Joseph Gomes**[2], **Kyle A Beauchamp**[3], **Teresa Head-Gordon**[4,5], **Julia E Rice**[6], **William C Swope**[6], **Todd J Martínez**[2,7,8], **Vijay S Pande**[2,9]

[1]Department of Chemistry, University of California, Davis, Davis, California 95616, United States.

[2]Department of Chemistry, Stanford University, Stanford, California 94305, United States.

[3]Counsyl, Inc., South San Francisco, California 94080, United States.

[4]Departments of Chemistry, Bioengineering, Chemical and Biomolecular Engineering, and Kenneth S. Pitzer Center for Theoretical Chemistry, University of California, Berkeley, Berkeley, California 94720, United States.

[5]Chemical Sciences Division, Physical Biosciences Division, Lawrence Berkeley National Laboratory, Berkeley, California 94720, United States.

[6]IBM Almaden Research Center, IBM Research, San Jose, California 95120, United States.

[7]PULSE Institute, Stanford University, Stanford, California 94305, United States.

[8]SLAC National Accelerator Laboratory, Menlo Park, California 94025, United States.

[9]Departments of Computer Science, Structural Biology, and Program in Biophysics, Stanford University, Stanford, California 94305, United States.

Abstract

The increasing availability of high-quality experimental data and first-principles calculations creates opportunities for developing more accurate empirical force fields for simulation of proteins. We developed the AMBER-FB15 protein force field by building a high-quality quantum chemical data set consisting of comprehensive potential energy scans and employing the ForceBalance software package for parameter optimization. The optimized potential surface allows for more significant thermodynamic fluctuations away from local minima. In validation studies where simulation results are compared to experimental measurements, AMBER-FB15 in combination with the updated TIP3P-FB water model predicts equilibrium properties with

* pande@stanford.edu .

Disclosure

KAB is currently an employee of Counsyl, Inc.

VSP is a consultant and SAB member of Schrodinger, LLC and Globavir, sits on the Board of Directors of Omada Health, and is a General Partner at Andreessen Horowitz.

TJM is a co-founder of PetaChem, LLC.

Supporting Information Available. Scatter plots of original and optimized force field parameters for AMBER-FB15; RMSD time series for simulated proteins not shown in the main text; NMR S^2 order parameter calculation for lysozyme with thresholded experimental value; NMR ^3J couplings for ubiquitin and NTL9; summaries of RMS errors in predicted chemical shifts; temperature dependence plots for AAQAA and CLN025 with 4-point water models; additional tables and figures describing protein-water interaction energies.

equivalent accuracy, and temperature dependent properties with significantly improved accuracy, in comparison with published models. We also discuss the effect of changing the protein force field and water model on the simulation results.

Graphical Abstract

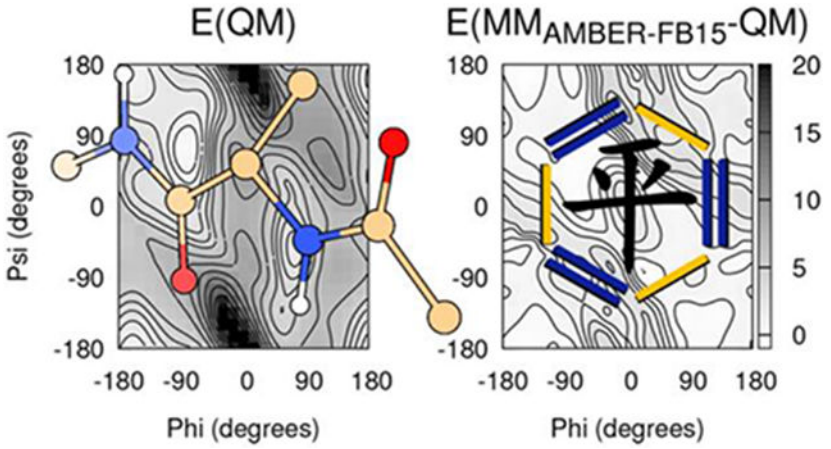

INTRODUCTION

Molecular Dynamics (MD) simulations have demonstrated high utility for the functional study of biomolecular systems. The degree of spatial and temporal resolution afforded by this technique allows for atomic-scale analysis of structure, dynamics, and function. In order to achieve time scales relevant to biological processes, a classical interaction potential, or force field, is typically used. Although approximate, these models are a vital part of developing the mechanistic, thermodynamic, and kinetic understanding of biological phenomena including but not limited to enzyme catalysis[1-10], protein folding[11-18], protein-ligand binding,[19-26] and protein conformational change.[27-33] The results of these studies strongly depend on the accuracy of the underlying force field. While there have been noteworthy simulations on protein dynamics using a quantum chemical potential energy surface,[34-36] these are still incapable of realizing dynamics on the biologically relevant timescales (ns and beyond) for larger proteins (200 residues and beyond). Therefore, the development of accurate empirical force fields is still crucial for computational biomolecular simulation.

The conceptual development of the consistent force field is credited to Lifson who proposed that the interactions between atoms could be described using an energy function and a small set of transferable empirical parameters. In 1967, Lifson, Warshel and Levitt successfully derived and parameterized the first force field.[37] In 1969, this idea was implemented by Levitt with the first computer simulation of a protein.[38]

Important to the future of condensed phase force fields was the development of the Optimized Potentials for Liquid Simulations (OPLS) model proposed by Jorgenson in the 1980s.[39] Here the nonbonded interactions were derived by fitting to experimental thermodynamic properties of organic liquids, a method which inspired parameterization

methodologies of the first generation of all-atom protein force fields. The CHARMM force field was also introduced in the 1980s along with the molecular dynamics program of the same name,[40] and the force field has undergone several significant revisions in recent years as experimental and ab initio data have improved.[41-43] As subsequent developments are too numerous to describe here, we refer the reader to some more comprehensive reviews.[44-47]

One of the first force fields capable of all-atom simulations of proteins in water is of the AMBER type and referred to as ff94.[48] This model approximates the energy of a system of molecules as a sum of terms including harmonic bonds, harmonic angles, electrostatic interactions, Lennard-Jones repulsion and dispersion interactions, and dihedral energy terms for adjusting the energy profiles of bond rotations. Harmonic bond and angle terms were optimized to reproduce experimental normal mode frequencies by fitting to structural and vibrational frequency data on small molecule fragments of amino and nucleic acids. The atom-centered point charges were fit using Kollman's RESP method, which aims to reproduce the electrostatic potential of a target molecule to calculations at the HF/6-31G* quantum level of theory;[49] this process was accelerated significantly using Bayly's semiempirical AM1-BCC approach.[50-51] The Lennard-Jones parameters were fit in order to reproduce densities and enthalpies of vaporization in simulations of organic liquids (as was done for OPLS). The dihedral parameters were fit using relative energies of alanine and glycine dipeptide conformers calculated via quantum mechanical (QM) methods at the MP2/6-31G* level.

The subsequent widely adopted major iterations of the AMBER type force field have carried over the functional form and most parameters from the original ff94 model. These more recent developments focused primarily on improving protein secondary structure representation via the successive refitting of the ff94 dihedral parameters. The torsions in ff94 applied equally to all quartets of atoms around a bond between two atom types; the parameters were fit to a set of experimental small molecule barrier heights. The ff99 force field[52] improved upon this approach by introducing explicit four atom dihedral terms that were fit to a larger set of small molecules, as well as a reference set of alanine tetrapeptide conformers. The ff99SB force field[53] was introduced by Hornak and Simmerling to improve conformational preferences for glycine and address known deficiencies of previous AMBER force fields such as over-stabilization of α-helices.[54] The amino acid backbone dihedrals for glycine and alanine were refit using a grid-based conformational scan of alanine and glycine tetrapeptides. In ff99 and ff99SB, the other protein parameter types were left unmodified from ff94. The ff99SB-ILDN[55] force field of Shaw and coworkers introduced explicit side chain parameters for four specific residue types (isoleucine, leucine, aspartate, and asparagine). The explicit side chain parameters were fit to grid-based conformational scans calculated using second-order Møller-Plesset perturbation theory with the resolution of the identity approximation[56-57] (RI-MP2) and a correlation-consistent augmented triple zeta basis set[58] (aug-cc-pVTZ), and validated by calculating NMR observables from simulation trajectories and comparing to experiment. The ff99SB-NMR force field of Li and Bruschweiler was explicitly fit to NMR data by matching chemical shift predictions from MD trajectories to experiment.[59] Although each successive modifications of the ff99 force field led to further improvements in secondary structure, the temperature dependence of partial folding remained a major limitation for these models.[60]

Today, researchers are looking in the directions of replacing the point charge model carried over from ff94 with new fixed-charge models and non-additive electrostatic potentials that include explicit polarization. The implicitly polarized charge model[61] found in the ff15ipq[62] force fields treats the point charges of a target molecule as a sum of the charges calculated in vacuum and a perturbation of these charges caused by the presence of explicit solvent molecules, and in this way accounts for electrostatic polarization in a nonpolarizable model. The addition of polarizability in the form of Drude particles[63] or induced dipoles[64] produces a more physically realistic model of electrostatic polarization; however, these models incur a significantly greater computational cost which limits the timescales that are accessible compared with fixed-charge models. These new electrostatic models show great promise for improving the accuracy of the protein energy potential. However, protein force fields that incorporate these electrostatic models require refitting of the other bonded and nonbonded parameter types, and they have yet to be tested to the same extent as the RESP model. It is likely that fine-tuning of bonded and van der Waals interactions using high quality *ab initio* data will continue to be an essential part of developing future generations of protein force fields.

In this work our goal is to assess the limits of accuracy that can be attained by fitting intramolecular bond, angle, and dihedral parameters to QM calculations without modifying the functional form and nonbonded parameters, which we expect will complement efforts currently being undertaken to improve the nonbonded part. We systematically explore the modification of bond, angle, and dihedral parameters, taking the ff99SB functional form and parameter set as a starting point. We introduce a new potential energy scanning method to build an improved data set of dipeptide conformations and provide unprecedented coverage of the conformational space. The parameter optimization was done using ForceBalance,[65] an open-source software package designed to enable reproducible and systematic force field development.

The new parameter set is validated by calculating thermodynamic observables from protein simulations and comparing to experiment. We find that the new parameter set performs equally well as the previous models for equilibrium properties, where previous models gave good agreement with experiment, and gives superior performance for temperature dependence, where previous models perform poorly. Our main finding from the parameter re-optimization is that the ff99SB, and related similarly derived models, overestimate the steepness of potential energy basins, which explains why they predict the correct equilibrium structures, but may lead to problems when simulating conformational changes or deviations from these structures as observed in our subsequent validation studies.

Our validation testing includes a comparison of protein force fields combined with four water models: the TIP3P model most widely used in protein simulations, the updated and more accurate TIP3P-FB model[65], and the four-point TIP4P-Ew[66] and TIP4P-FB[65] models. TIP4P-Ew is a four-point water model developed for use with the particle mesh Ewald electrostatics method[67] that is ubiquitous today, and was among the first water models parameterized to accurately reproduce the temperature dependence of the density.[66] The TIP3P-FB and TIP4P-FB models, developed ten years later, use the same functional form as TIP3P and TIP4P-Ew (respectively) and were systematically parameterized to

reproduce the temperature and pressure dependence of a wide range of thermodynamic properties.[65] Despite the advances made in water models over the last two decades, the protein force fields have largely followed historical precedent in that they are developed and tested for use with the TIP3P model, which raises interesting questions of how the simulation accuracy may be affected if the water model is changed. Here, our validation studies show that different force field / water model combinations produce widely varying temperature dependence properties of the protein, and combining AMBER-FB15 with TIP3P-FB produces the best agreement with experiment, despite the fact that the protein intermolecular parameters were not optimized. We discuss some interesting patterns in how different water models affect protein stability. We also describe common limitations of all tested models, which include underestimation of the slopes of protein melting curves and overly collapsed denatured state ensembles, highlighting the necessity of improved descriptions of nonbonded interactions.

The force field combination AMBER-FB15/TIP3P-FB is recommended for general-purpose simulations of proteins, particularly in situations where fluctuations away from equilibrium and temperature dependence are expected to play an important role. Additionally, the *ab initio* data set used to parameterize AMBER-FB15 has been made publicly available online,[68] and we expect it to be useful for force field development efforts in the community.

THEORY

AMBER functional form.

The AMBER99SB protein force field (abbreviated as A99SB) is the starting point of the parameterization in this work; it consists of the simple and well-known functional form put forth in AMBER94 (here referred to as the AMBER functional form), the AMBER99 parameter set, and the “SB” correction to the protein backbone dihedral parameters.[53] In the AMBER functional form, the total potential energy of the system is written as a sum of bonded and nonbonded contributions:

$$
\begin{aligned}
E &= E_{\text{bond}} + E_{\text{angle}} + E_{\text{dihedral}} + E_{\text{improper}} + E_{\text{vdW}} + E_{\text{ele}}, \\
E_{\text{bond}} &= \sum_{i,j \in \text{bonds}} \frac{k^b_{ij}}{2}\left(r_{ij} - r^0_{ij}\right)^2, \quad E_{\text{angle}} = \sum_{i,j,k \in \text{angles}} \frac{k^\theta_{ijk}}{2}\left(\theta_{ijk} - \theta^0_{ijk}\right)^2, \\
E_{\text{dihedral}} &= \sum_{i,j,k,l \in \text{dihedrals}} \sum_{n=1}^{6} k^\phi_{ijkl,n}\left(1 + \cos\left(n\phi_{ijkl} - \phi^0_{ijkl,n}\right)\right), \\
E_{\text{improper}} &= \sum_{i,j,k,l \in \text{impropers}} k^\phi_{ijkl,2}\left(1 + \cos\left(2\phi_{ijkl}\right)\right), \\
E_{\text{vdW}} &= \sum_{i,j \in \text{nonbonded}} 4\varepsilon_{ij}\left[-\left(\frac{\sigma_{ij}}{r_{ij}}\right)^6 + \left(\frac{\sigma_{ij}}{r_{ij}}\right)^{12}\right] \\
E_{\text{ele}} &= \sum_{i,j \in \text{nonbonded}} \frac{q_i q_j}{r_{ij}},
\end{aligned}
\tag{1}
$$

where i, j, k, l are atomic indices and r_{ij}, θ_{ijk}, ϕ_{ijkl} are functions of the atomic coordinates. The empirical parameters for bonded interactions are denoted as k^b_{ij}, r^0_{ij}, k^θ_{ijk}, θ^0_{ijk}, $k^\phi_{ijkl,n}$, $\phi^0_{ijkl,n}$ and depend on the *atom types* of the atoms involved. This work focuses on optimizing the bonded parameters, in some cases defining new atom types to increase the size of the parameter space.

In the nonbonded interactions involving pairs of atoms separated by 3 or more bonds, the pairwise Lennard-Jones parameters σ_{ij} and ε_{ij} are derived from those of individual atom types (σ_i and ε_i) via the Lorentz-Berthelot combining rules, and the atomic partial charges q_i are defined for each atom in each amino acid. These parameters are not modified in this work. The vdW and electrostatic interactions between pairs of atoms separated by exactly three bonds (i.e. "1-4 pairs") are reduced by factors of 1.2 and 2.0, respectively; the 1-4 interactions are nominally considered to be a kind of bonded interaction, but they are also not modified in this work.

Reference data set.

We constructed a database of *ab initio* calculations, summarized in Table 1, consisting of single-point energies, nuclear gradients, and vibrational modes calculated for the blocked dipeptides ACE-X-NME containing one amino acid side chain. This database is further supplemented by additional single-point energies and gradients evaluated at optimized geometries using intermediate force field parameter sets, described later. All energy and gradient values in the database were respectively computed at the RI-MP2/CBS and RI-MP2/aug-cc-pVTZ levels of theory; the calculations were performed in the gas phase. For each dipeptide, a 24x24 grid of structures was generated by constraining the backbone dihedral angles φ and ψ at 15-degree increments and minimizing the energy in the orthogonal degrees of freedom; a second grid for the side chain dihedral angles χ_1 and χ_2 was carried out for all amino acids with a side chain, except for valine and deprotonated cysteine (CYM) where the second grid uses φ and χ_1 instead.

Beyond the simplest dipeptides (i.e. glycine and alanine), the potential energy surfaces contain many local minima that cannot be comprehensively searched using local optimization methods. Moreover, a sequence of constrained geometry optimizations through a full rotation of a dihedral angle may not return to the starting structure, analogous to turning a corkscrew embedded in a cork. This hysteresis is a consequence of the many orthogonal degrees of freedom that are only locally optimized using the previous structure as the initial guess. Our approach for scanning the potential surface attempts to find the lowest-energy local minimum in the orthogonal degrees of freedom, as they are likely to carry a higher thermodynamic weight in the protein. To this end we developed the following procedure to explore the conformational space using lower levels of theory:

1. Obtain a four-dimensional grid of structures using gas-phase simulated annealing simulations and the AMOEBA13 polarizable force field; the number of grid points was 12, 12, 6, 6 for φ, ψ, χ_1 and χ_2 respectively, giving a total of 5184 points for each amino acid.

2. For each structure on the four-dimensional grid, perform a MP2/6-31+G* geometry optimization with φ, ψ, χ_1 and χ_2 constrained.

3. For two chosen dihedral angles (e.g. φ, ψ), map the four-dimensional grid of structures to the two-dimensional grid and record the structure with the lowest energy, denoted by $q_{\varphi,\psi}$, $E_{\varphi,\psi}$. Note that after step 2, only one structure for each (φ, ψ) grid point is recorded out of a total of 36.

4. For each 2-D grid point (φ, ψ) containing a new lowest energy structure, initialize four MP2/6-31+G* geometry optimizations with new dihedral angle constraints $\varphi \pm \frac{\pi}{12}$, $\psi \pm \frac{\pi}{12}$.

5. Repeat steps 3 and 4 until no new lowest-energy structures are found. The end result is a 24x24 grid of structures with a resolution of $\frac{\pi}{12}$.

In each iteration of steps 3 and 4, each grid point with a new lowest-energy structure is used to launch four new geometry optimizations at the neighboring grid points, and the procedure is carried out recursively until no more lowest-energy structures are found. The number of times the recursive procedure was iterated depended on the side chain flexibility of the amino acid, ranging from 6 (ALA, GLY) to 24 (GLU). At the conclusion of the calculation, each structure is minimized over the initial configurations of its four neighboring structures, and this condition is satisfied for the entire surface; the result is a grid of structures where the energy changes by as little as possible between the grid points, although the geometry may change significantly along the orthogonal degrees of freedom. Following this, each structure is re-optimized at the RI-MP2/aug-cc-pVDZ level with the same dihedral constraints. A single RI-MP2/aug-cc-pVQZ calculation at the optimized geometry provides the means to estimate the energy in the MP2/CBS limit using Helgaker's two-point extrapolation.[69] The gradient computed at the RI-MP2/aug-cc-pVTZ level is also added to this data set.

We also carried out a geometry optimization and frequency calculation at the RI-MP2/aug-cc-pVTZ level for the overall lowest-energy structure and scaled the frequencies using standard scaling factors.[70] Two separate scaling factors were used – 0.960 for high frequencies and 1.012 for low frequencies, using 1000 cm^{-1} to distinguish the high-frequency and low-frequency regions.

In frequency regions near the dividing line, using these multiplicative scaling factors could cause vibrational frequencies to switch order. To prevent this from happening, the frequency shifts Δ_h for vibrations ν_h above 1000 cm^{-1} are attenuated with the following formula:

$$\Delta_h = \Delta_{h,0} s_h, \text{ where } \Delta_{h,0} = (0.96 - 1.0)\nu_h, \text{ and } s_h = \frac{\nu_h - \nu_d}{\nu_h - 0.96\nu_d}. \quad (2)$$

When ν_h approaches the dividing frequency ν_d = 1000 cm^{-1}, the attenuating factor ensures that the scaled frequency never falls below the dividing frequency. A similar attenuating factor is defined for vibrational frequencies ν_l below 1000 cm^{-1}:

$$\Delta_l = \Delta_{l,0} s_l \text{ where } \Delta_{l,0} = (1.012 - 1.0)\nu_l, \text{ and } s_l = \frac{\nu_l - \nu_d}{\nu_l - 1.012\nu_d}. \quad (3)$$

Parameter optimization.

The parameters were optimized using the ForceBalance software package.[65, 71-72] ForceBalance provides a framework where the differences between force field predictions and provided reference data are used to construct a weighted least-squares objective function and its derivatives. A regularization term (penalty function) is applied to prevent large parameter deviations where reference data is insufficient or the force field contains linear dependencies. The calculation is fully specified by:

(1) the functional form of the force field, parameter space (i.e. selection of which parameters to optimize and their interdependencies) and initial parameter values,

(2) the *targets* and their weights that contribute to the objective function,

(3) the *prior widths* that constrain the parameter deviations from their initial values, and

(4) the optimization algorithm that minimizes the objective function.

A major advantage of using ForceBalance is that the calculation is precisely specified and systematically carried out, ensuring that the results are reproducible and significantly reducing the effort involved when repeating the calculation with any component added or changed.

We used the functional form and initial parameters from the AMBER99SB force field; the choice of parameter space was decided by exploring the possible combinations of options in tuning the bond, angle, and torsional parameters, as described in the results and discussion section. We also explored defining independent dihedral parameters for amino acid side chains, which goes beyond the flexibility of the original AMBER99SB model. The extension of AMBER using side chain specific parameters has previously been explored in models such as AMBER99SB-ILDN, RSFF2[73] and AMBER14SB.[74]

The objective function is defined as a function of the differences between the force field predictions and the reference data, plus a regularization term that penalizes large parameter deviations from the initial values. The three types of targets and penalty term are combined as:

$$\chi^2 = \sum_{i=1}^{N_{\text{grids}}} \chi^2_{\text{grid};\,i} + \sum_{i=1}^{N_{AA}} \chi^2_{\text{vib};\,i} + 4\sum_{i=1}^{N'_{AA}} \chi^2_{\text{MM}_{\text{opt}};\,i} + \sum_{i=1}^{N_{\text{prm}}} \left(\frac{\alpha_i - \alpha_i^0}{p_i}\right)^2. \quad (4)$$

The first term χ^2_{grid} represents the contributions from the energies and gradients evaluated over a two-dimensional dihedral grid:

$$\chi^2_{\text{grid}} = \left\langle w_E \frac{\left(E_{MM} - E_{QM}\right)^2}{\left\langle E^2_{QM}\right\rangle - \left\langle E_{QM}\right\rangle^2} + \frac{w_F}{3N_{\text{atom}}} \frac{\left| F_{MM} - F_{QM} \right|^2}{\left\langle \left| F_{QM} \right|^2 \right\rangle} \right\rangle \tag{5}$$

where E_{MM}, F_{MM} and E_{QM}, F_{QM} represent the energies and forces determined using the MM force field and QM reference set, respectively. The MM and QM energies are both referenced to the structure with the lowest QM energy. Similarly, $w_E = 1.0$ and $w_F = 0.1$ are weighting factors for the energy and force error terms. The angle brackets denote a weighted average over the points, and the denominators ensure that the objective function has no physical units and the quantities are expressed as relative errors. The weighted average is given as:

$$\langle x \rangle \equiv \frac{\sum_{i=1}^{N_{pts}} w\left(E_{i,QM}\right) A\left(E_{i,MM} - E_{i,QM}\right) x_i}{\sum_{i=1}^{N_{pts}} w\left(E_{i,QM}\right) A\left(E_{i,MM} - E_{i,QM}\right)}, \tag{6}$$

where the factors $w(E)$ and $A(E_{MM} - E_{QM})$ are given by:

$$w(E) = \begin{cases} D^{-1}, E \le D \\ \left(D^2 + (E-D)^2\right)^{-\frac{1}{2}}, E > D \\ 0, E > U \end{cases} ; \quad A(\Delta) = \begin{cases} 1, \Delta \ge 0 \\ 100, \Delta < 0 \end{cases} \tag{7}$$

$w(E)$ is a decreasing function of the reference energy above the minimum, plotted in Figure 1. $D = 5$ kcal/mol is the energy threshold below which $w(E)$ is a constant; above the threshold, $w(E)$ becomes inversely proportional to the reference energy. $U = 20$ kcal/mol is the upper energy cutoff above which the weight is set to zero. $A(E_{MM} - E_{QM})$ depends on the sign of the MM-QM energy difference and heavily penalizes MM energies that are lower than the QM energies. This reflects our experience that the positive and negative errors in the fit result in asymmetric effects on the simulations. Configurations with negative $E_{MM} - E_{QM}$ have a spuriously large thermodynamic weight and are more likely to appear during MM sampling, which could shift the peaks of the distribution and lead to severe errors such as incorrect equilibrium structures. On the other hand, configurations with positive $E_{MM} - E_{QM}$ have a spuriously small weight in the MM ensemble and underestimate portions of the distribution; this could result in overestimation of barriers and underestimation of fluctuations, which are (in a sense) higher-order errors than incorrect equilibrium averages. Thus, enforcing $E_{MM} - E_{QM}$ to be nonnegative everywhere and using a weight function that decays with E_{QM} forces the fitting errors into the high-energy regions, where we expect the impacts on the thermodynamic properties to be the smallest.

The second term χ^2_{vib} represents the contributions from the vibrational frequencies evaluated over the 20 standard amino acids:

$$\chi^2_{\text{vib}} = \frac{1}{N_{\text{modes}}} \sum_{i=1}^{N_{\text{modes}}} \left(\frac{v_{i,MM} - v_{i,QM}}{100\,\text{cm}^{-1}} \right)^2 \quad (8)$$

The QM vibrational modes are ordered by increasing frequency, whereas the corresponding MM vibrational mode is chosen to have the largest absolute value of the dot product with the QM vibrational eigenvector. Unlike the energy and gradient calculations, the MM energy is minimized prior to calculating the vibrational modes. Comparisons between eigencomponents allows for relatively even weighting of high and low frequency modes. Although comparing the force constant matrices would be more straightforward, it may overrepresent the higher frequency modes that correspond to larger matrix elements.

The third term in the objective function addresses the appearance of spurious energy minima in the MM force field in parts of configuration space not covered by the grid of structures. This term consists of energies and gradients evaluated at MM-optimized structures as in Equation (6), but without energy-dependent weights. We fully optimized each structure on the grid using the MM force field without constraints and clustered the structures with a heavy-atom root-mean-square deviation (RMSD) cutoff of 0.1 Angstrom, leading to a small number of cluster centers for each amino acid (< 50). These structures were used to calculate MP2/CBS energies and MP2/aTZ gradients that were added to the objective function. Because updating the force field parameters changes the MM energy surface and the locations of minima, this cycle can be repeated to eliminate spurious minima that appear for the new parameter set.

The fourth term in the objective function is the regularization term that penalizes parameter deviations from their initial values. Since the force field parameters have different physical unit systems, the parameter deviations must be placed on the same footing by rescaling prior to computing the penalty function. The penalty function corresponds to a prior distribution in a Bayesian interpretation, and thus the rescaling factors for parameter deviations are equivalent to the prior widths. The results of the optimization do depend on the choice of prior widths, but in a much less sensitive way compared to the force field parameters themselves. Because the bond and angle terms are intended to model small harmonic displacements away from the lowest-energy structure, we chose small prior widths (approximately 10-20% of the parameters' intrinsic size) to enforce small parameter changes in the optimization. On the other hand, the dihedral terms are expected to vary more widely, as they represent a compromise between the bonded and nonbonded parts of the force field. We thus chose the prior widths to be on the same order as the parameter themselves. The full set of prior widths used in the optimization is given in Table 2.

The objective function was minimized using a variation of the Levenberg trust-radius method[75-78] implemented in ForceBalance. A parameter update ($\mathbf{k}_{n+1} - \mathbf{k}_n$) is calculated as:

$$\mathbf{k}_{n+1} - \mathbf{k}_n = \left[\mathbf{H} \mid_{\mathbf{k}_n} + (\lambda - 1)^2 \mathbf{I} \right]^{-1} \mathbf{G} \mid_{\mathbf{k}_n} \quad (9)$$

where $G_i \equiv \frac{\partial}{\partial k_i}\chi^2$ and $H_{ij} \equiv \frac{\partial^2}{\partial k_i \partial k_j}\chi^2$ are the gradient and Hessian matrix of the objective function in parameter space, and λ is a parameter that affects the length of the optimization step. The Hessian is approximated using the Gauss-Newton method. For the calculations in this paper, the objective function is much less expensive to evaluate than its derivatives – so a line search over λ is performed rather than taking an optimization step of a fixed length. ForceBalance uses the Brent method as implemented in SciPy[79] to perform the line search. The quadratic form of the coefficient $(\lambda - 1)^2$ maps all λ values on the real line to nonnegative values and ensures that the line search is well behaved.

COMPUTATIONAL METHODS

The *ab initio* reference calculations were carried out in a workflow involving several software packages. The initial high-dimensional dihedral grid of structures was generated from restrained simulated annealing simulations using the AMOEBA protein force field as implemented in TINKER.[80] The recursive search over the two-dimensional dihedral grids was performed using a Python program that interfaces with the Q-Chem 4.1 quantum chemistry package[81-82] and uses the Work Queue distributed computing library[83] to manage a large number of Q-Chem calculations running in parallel. The calculations of final optimized structures, energies and gradients were performed in Psi4.[84] Frequencies were obtained in Psi4 via numerical differentiation of the analytic gradients.

The parameterization calculations were performed using ForceBalance via an interface to GROMACS 4.6.5,[85] and contained two fundamental types of MM calculations – single-point energy / gradient evaluations, and frequency calculations. In the frequency calculations, the MM energy was fully minimized using the L-BFGS algorithm prior to calculating the Hessian. ForceBalance also uses the Work Queue library to evaluate individual *targets* in parallel, providing a significant speed-up compared to running all of the MM calculations sequentially.

The validation calculations were performed using multiple software packages. The equilibrium sampling simulations initialized from the crystal structure were carried out using GROMACS 4.6.5 running on standard Linux HPC hardware. The analyses of the equilibrium simulations to calculate RMSD from the crystal structure and NMR scalar couplings / chemical shifts were carried out using the GROMACS analysis tools, the MDTraj trajectory analysis package,[86] and the ShiftX2 chemical shift prediction software[87].

The temperature replica exchange simulations were set up using the ParmEd software package[88] to convert the GROMACS topology files to AMBER format, carried out using the GPU-accelerated version of AMBER14[89] running on the OLCF Titan supercomputer, and analyzed using the cpptraj[90] and MDTraj[91] software packages. The simulations of the denatured state ensemble were carried out on the Open Science Grid (OSG), a distributed computing network that utilizes donated idle CPU cycles from research computing facilities.[92]

RESULTS AND DISCUSSION

Choice of optimization parameters.

We assessed the significance of optimizing different types of parameters by testing the following choices: (1) including bond and angle parameters, (2) allowing side chain torsions to take on distinct parameter values, and (3) including equilibrium geometry parameters in addition to the force constants. We ran several optimizations using a simplified version of the objective function where only the (φ, ψ) dihedral scans were included (first row of Table 1). The results demonstrate that tuning the backbone dihedral parameters have a significant effect on decreasing the objective function (Table 3). Perhaps more surprising is the effect of bond and angle parameters; the first and third rows of Table 3 show that including the bond and angle force constants lower the objective function by ~30% compared to using only the dihedral force constants. Allowing the equilibrium geometry parameters to be optimized results in a further 50% decrease in the objective function as shown in the fifth row of Table 3. Based on these results, we decided to allow all parameter types to vary in our optimizations.

The model named A99SB-V is the optimized result using all of the A99SB bonded parameters and the data in Table 1. After adding some parameters corresponding to alternative protonation states of amino acids, the total number of adjustable parameters in A99SB-V was 434, and the mean unsigned error (MUE) of the potential across all of the dihedral scans was 1.90 kcal/mol. We also developed a variant of this force field where the side chain torsion parameters for different amino acids were all allowed to vary independently; this led to a decrease of 37% in the objective function, but the number of parameters increased greatly to 1406. Because this force field reproduced experimental results more accurately than A99SB-V and several other models in the validation calculations, we named it AMBER-FB15 and recommend it here for broader use.

Optimized parameter values.

Figures S1-S3 in the Supporting Information show the original and optimized parameter values in AMBER-FB15 grouped by parameter type. The optimized equilibrium bond and angle parameters are all within 5% of their initial values and fall very close to the straight line. Bond and angle force constants show slightly larger deviations; some force constants involving the amide bond are reduced by up to 10% from their initial values. The torsion phases and amplitudes are more widely distributed, largely because the initial guesses for side-chain parameters are set to zero. With few exceptions, the equilibrium torsion phases fall within $\frac{\pi}{6}$ radians (30 degrees) of their initial values, and the torsion amplitudes seldom change by more than 4 kJ/mol (1.0 kcal/mol). The largest parameter deviations are observed for arginine and lysine, which possess charged side chains; this is expected due to the especially strong electrostatic interactions in the gas-phase QM calculations, which contributes large terms to the objective function. We note in passing that the usage of gas-phase QM data is most likely to fail for charged systems, but choosing the most appropriate QM method to fit a condensed-phase fixed charge model remains an important challenge.[61]

Quality of fit.

Figure 1 shows the potential surface of alanine dipeptide evaluated at the constrained energy minima. As expected, AMBER-FB15 produces a closer fit to the QM energy surface relative to A99SB-ILDN (equivalent to A99SB for alanine). Comparison of the QM and MM surfaces reveals that A99SB-ILDN fits the low-energy regions (in blue) much more accurately than the high-energy regions (in red), and high-energy regions are systematically overpredicted. By contrast, AMBER-FB15 significantly reduces (but does not eliminate) the overprediction of the energy, and the low-energy basins with energy less than 5 kcal/mol above the minimum are significantly broadened. We expect that the broader energy basins in low-energy regions will lead to larger thermodynamic fluctuations at finite temperatures, which may result in more accurate predictions (as explored in the validation simulations).

Figure 2 shows the comparison of QM and MM energies at the local minima of the optimized force field for threonine dipeptide. The initial parameter set (red crosses) predicts the relative energies with a RMS error of 2.16 kcal/mol, and several local minima are within 2 kcal/mol of the lowest-energy structure; by contrast the QM relative energies are significantly higher, ranging between 2 and 6 kcal/mol above the minimum. These local minima with spuriously low relative energies are biased towards higher probability in finite-temperature simulations, which could adversely perturb the equilibrium structure. These local minima are added to the objective function (third term in Equation (4)) to obtain a new set of parameters, which predicts a new set of local minima with relative energies that match the QM calculations much more closely (yellow crosses). Repeating the addition of local minima to the objective function leads to smaller improvements in the predicted relative energies (blue crosses), and the resulting parameter set is kept as the final version.

Equilibrium properties.—After a force field is developed, the predictive power of the model is validated using a set of test properties not used during the fitting procedure. In order to assess the ability of AMBER-FB15 to reproduce equilibrium properties of folded proteins, we ran simulations of 8 proteins: the third IgG-binding domain from streptococcal protein G, abbreviated as *GB3* (PDB ID: 1IGD), *acetyltransferase* from the COG2388 family (2EVN), *lambda repressor* taken from the repressor-operator complex (1LMB), *lysozyme* from bacteriophage lambda (1AM7), N-terminal Domain of Ribosomal Protein L9 or *NTL9* (2HBA), a variant of the *Trp-cage* miniprotein (2JOF), *ubiquitin* (1UBQ), and chicken villin subdomain HP-35 or *villin headpiece* (2F4K). Each protein was simulated at 298.15 K using 7 force fields and 4 water models. All proteins were solvated in a cubic water box with a side length of 62 Å. Na^+ and Cl^- ions were added to neutralize the proteins using the parameters of Åqvist;[93] the ubiquitin simulations had 12 additional ion pairs corresponding to an ionic strength of ~50 mM. For each simulation, the RMSD of the protein backbone to the PDB reference was computed using the residue intervals specified in Table S1, and the RMSD probability density function estimated via a kernel density estimate (KDE). In order to separate thermodynamic fluctuations from shifts in the equilibrium structure, we calculated the Cartesian-averaged protein backbone coordinates (after alignment to remove translation and rotation) and calculated the RMSD to the crystal structure; these values are typically lower than mean RMSD values. This data is illustrated for three proteins in Figure 3, and the rest are provided in Figure S4. Two protonation states

of lysozyme were considered – one state is determined using the pKa values of the amino acids, and the other is determined using the H++ pKa prediction software;[94] the simulation results were not significantly different and only the H++ simulation results are shown here. Each of the 252 simulations was performed for at least 300 ns with an average trajectory length of 500 ns.

Simulating a protein in water at ambient conditions may not reproduce the crystallographic structure exactly, due to differences in the environment and thermodynamic ensemble. However, crystal structures are often the best structural data available, and it is reasonable to assume that proteins in water stay reasonably close to the crystal structure unless experiments show strong evidence to the contrary. Thus, the RMSD of the simulation trajectory to the crystal structure is routinely considered as an important qualitative validation test of a protein force field, and simulations that deviate significantly from the crystal structure in a short time (i.e. on the sub-microsecond timescale) are interpreted as evidence of force field errors.

Figure 3 shows the RMSD time series for three proteins simulated using four combinations of the protein force field and water model. The protein remains folded in all simulations, and the simulations differ in terms of the overall RMSD to the crystal structure. In the case of ubiquitin, all models have nearly identical RMSD distributions, except for AMBER-FB15/TIP3P-FB which has a small shoulder in the distribution indicating more flexibility in the backbone (also see Supporting Figure S4). In lysozyme and GB3, AMBER-FB15 predicts an RMSD value in between that of A99SB-ILDN and A99SB-NMR; when the water model is changed to TIP3P-FB, the RMSD distribution is shifted to lower values. In all of the simulations except for acetyltransferase, the averaged backbone Cartesian coordinates of the AMBER-FB15/TIP3P-FB remains very close to the crystal structure with a RMSD of 1.0 Å or less. The RMSD distribution for lysozyme is significantly broader than ubiquitin and GB3, and the A99SB-ILDN simulation possesses some bimodal character; this may indicate larger conformational changes on timescales exceeding microseconds that have not been fully sampled in our calculations.

To enrich our understanding of model dependence on equilibrium stability, Lipari-Szabo S^2 order parameters were computed for proteins and compared to the available experimental data. Previous studies have shown that simulation lengths exceeding 100 ns are required for accurate estimation of these order parameters,[95] a condition that is satisfied by our calculations. These simulated observables were determined from the trajectories using the isotropic reorientational eigenmode dynamics[96] (iRED) as implemented in the cpptraj program[90] for windows of length 2, 4, and 8 ns. The per-residue deviation from the experimental NMR measurements are shown in Figure 4. These order parameters measure the orientational disorder of the protein backbone N-H vectors on the sub-nanosecond timescale. For all three proteins simulated, we found AMBER-FB15 to produce lower S^2 values by 0.02–0.03 compared to A99SB-ILDN and A99SB-NMR. In the cases of ubiquitin and GB3, AMBER-FB15 predicts significantly lower mean signed errors (MSE), indicating that the increased disorder is consistent with experiment. AMBER-FB15/TIP3P-FB predicts the smallest root mean squared errors (RMSE) for these two proteins. In the case of lysozyme, the experimental measurements have many S^2 values in excess of 0.9, higher

than all of the simulated values; here AMBER-FB15 predicts the largest MSE although the RMSE is still very close to those of A99SB-ILDN and A99SB-NMR. An earlier study by Smith and coworkers applied an upper threshold of 0.9 to the experimental order parameters;[97-98] when using this threshold, all of the RMSE values are significantly reduced with AMBER-FB15 producing the lowest error (Figure S5).

The protein structure from equilibrium MD can also be related to NMR experiments using empirical relations to map the three-dimensional structure to the NMR observable. Three-bond J-couplings are often used to compare simulated dihedral angles to experiment; this requires the use of an empirical Karplus relation, which is developed by fitting the crystal structure backbone and side chain dihedral angles to the NMR observable. The comparison of calculated to experimental NMR observables is an important validation test, but perfect agreement is not expected due to the assumptions and residual errors of the empirical model. Furthermore, because the Karplus relations implicitly include some effects of dynamics in mapping the crystal structure to the solution NMR experiment, using molecular dynamics snapshots as an input to this mapping results in double-counting the effects of dynamics[99-100] which may lead to additional errors.

Figure 5 shows the RMS error of the computed NMR three-bond J-couplings compared to experiments for two proteins, bacteriophage lysozyme and GB3. The recommended model in this work (AMBER-FB15/TIP3P-FB) is compared to A99SB-ildn and A99SB-nmr, both with the TIP3P water model. From examining the left column, the AMBER-FB15/TIP3P-FB model predicts the backbone J-couplings of bacteriophage lysozyme in closer agreement with experiment. The right column shows that A99SB-ildn and AMBER-FB15 both have improved results over A99SB-nmr, which could be explained by the explicit parameterization of side chain torsional potentials. We also calculated J-couplings for two other proteins (ubiquitin and NTL9, Figure S6), and found small differences between the RMSE values compared to experiment on the order of 0.1 – 0.2 Hz. Although the J-couplings shown here were calculated using the Karplus parameters of Ruterjans and coworkers,[101-102] we note that the RMSE values change on the order of 0.1 when using the parameters of Bax and coworkers[103-104] and does not affect the qualitative interpretation of the results.

The NMR chemical shifts on ^{1}H, ^{13}C and ^{15}N can be predicted from MD trajectories using empirical models such as SHIFTX2,[87] which take into account a rather large number of geometric features and fitting parameters to represent the local chemical environment. Similar to Karplus relations for J-couplings, the chemical shift models are fitted using structural input from crystallography. The RMSE of the predicted chemical shifts are plotted in Figures S7 and S8. We observed that the prediction quality depends heavily on the protein, in contrast to the case of three-bond J-couplings. The RMSE is often within the range of the intrinsic error of SHIFTX2 itself; in an extreme case, the RMSE for ubiquitin is smaller than the SHIFTX2 intrinsic error, which corresponds to χ^2 statistics of less than one and does not reflect the differences between force fields in a meaningful way. From this, we concluded that the chemical shift predictions were insufficient to distinguish AMBER-FB15 from the literature models.

The results in this section show that AMBER-FB15 / TIP3P-FB does not degrade the accuracy of simulating proteins in their native structure at ambient conditions, which is an important validation test for any modern protein force field. Our claim is limited to the systems and time scales studied in this paper, but it lends important credibility to this model for future simulations of interesting biomolecular problems. Furthermore, equilibrium properties are no longer a frontier for protein force field development, with temperature dependence and characterization of the denatured state ensemble being much more important. We will focus our discussion on these important frontiers in the next section.

Temperature dependence.

Several of the most popular protein force fields in the past ten years have succeeded at reproducing equilibrium structures of folded proteins but failed to predict an accurate temperature dependence of the structural ensemble. In previous work, Best and Hummer proposed the A03* and A99SB* models which were directly fitted to reproduce helical fractions at finite temperature;[105] more recently, Wu and coworkers showed improved performance for temperature dependence adding extra 1-5 and 1-6 Lennard-Jones interaction terms and fitting the potentials to experimentally derived free energy distributions.[73] Here we consider the predicted temperature dependence of AMBER-FB15 for two model systems; Ac-$(AAQAA)_3$-NH_2 (abbreviated here as $AAQAA_3$), a 15-residue peptide with partial α-helical character at room temperature, and CLN025, a 10-residue peptide with mostly β-hairpin structure. These two proteins have a significant temperature dependence of the folded fraction in the range 280 – 370 C as measured by circular dichroism[106] and temperature-dependent infrared spectroscopy experiments.[107] The results presented in this section are taken from NVT replica exchange simulations as implemented in AMBER.[108-109] The published simulation results of several protein force fields from the last few years are also presented including FF12MC,[110] OPLS3[111], CHARMM22*,[112] and the AMBER force fields ff12sb and ff14sb.[74]

The left column of Figure 6 shows the temperature dependence of Ac-$(AAQAA)_3$-NH_2 for combinations of protein force fields and water models compared to experiment. Our results for published models show a high degree of consistency compared with existing protein force field validation studies of temperature dependence performed by Lindorff-Larsen and coworkers.[113] The top left and middle left panels compare seven protein force fields using the TIP3P and TIP3P-FB models respectively. The data indicates that protein force fields developed to reproduce equilibrium properties of folded proteins may fail to describe the temperature dependence of partially folded proteins; the A99SB and A99SB-ildn force fields significantly underestimate the α-helical fraction whereas A99SB-nmr significantly overestimates it. The two parameter sets discussed in this paper, A99SB-V and AMBER-FB15, also differ significantly in their temperature dependence. A99SB-V overestimates the helical fraction and behaves similarly to A99SB-nmr whereas AMBER-FB15 has a temperature dependence mostly consistent with the experiment.

The right column of Figure 6 shows temperature dependence plots for the CLN025 peptide, a small model of a β-hairpin. Due to the high cost of these simulations, we skipped the

older models (A96, A03 and A99SB) and compared four protein force fields only. The top right and middle right panels show that A99SB-ildn and A99SB-nmr both overestimate the folded fraction, in contrast to the results for Ac-$(AAQAA)_3$-NH_2 where A99SB-ildn and A99SB-nmr are on either side of the correct result. AMBER-FB15 again comes closest to reproducing the experimental result.

The bottom left panel of Figure 6 compares temperature trends of Ac-$(AAQAA)_3$-NH_2 using the AMBER-FB15 protein force field and four different water models. The choice of water model affects the helical content; the simulations using TIP3P predict the most helical content, followed by TIP3P-FB; the best agreement with experiment is given by TIP3P below 300K and TIP3P-FB above 300K. By contrast, the simulations using TIP4P-Ew and TIP4P-FB predict a much lower helical content. In a similar fashion, the bottom right panel of Figure 6 shows the temperature trends in the folded fraction of CLN025 using the AMBER-FB15 force field and four water models. The TIP3P simulations predict the highest folded fraction, followed by TIP3P-FB, then TIP4P-Ew and TIP4P-FB. Figure S9 shows that using the TIP4P-Ew and TIP4P-FB water models have the effect of decreasing the amount of protein structure for all seven protein force fields. The best overall agreement with experiment is given by the AMBER-FB15/TIP3P-FB simulations.

The effect of changing the water model on peptide stability is an interesting feature of the simulations. Clearly, the accuracy of the protein temperature dependence does not depend strongly on the accuracy of the water model, as both the TIP4P-Ew and TIP4P-FB models are highly accurate for computing the properties of water. The ability of protein simulations to accurately reproduce temperature dependence with TIP4P-Ew has been shown for model peptides where abundant NMR data is available, requiring changes in only one backbone dihedral parameter.[114] Moreover, the nonbonded protein parameters of the protein were not optimized, which will certainly have a strong effect on the temperature dependence. We expect that improved derivations of point charge models from quantum chemistry calculations[41, 61] and accompanying reparameterization of the Lennard-Jones interaction terms[115] will produce more accurate descriptions of temperature dependence for realistic water models; these efforts will likely require re-optimization of the torsion parameters, as the 1-4 electrostatics and Lennard-Jones terms contribute the major part of the torsional potential in the AMBER force field definition.[116] In light of all these considerations, it is still instructive to search for other trends in the water models that correlate well with the temperature dependence trends observed here.

When CLN025 is simulated with AMBER-FB15 (and when $AAQAA_3$ is simulated with A99SB-V), the helical/folded fraction takes on a wide range of values between 0.1 and 0.9; there is also a clear trend of peptide stability that goes as TIP3P > TIP3P-FB > TIP4P-Ew > TIP4P-FB. We could not find a significant correlation between the peptide stability and the basic properties of the water models, such as the internal energy or magnitude of the dipole moment. On the other hand, the peptide stability was significantly correlated with the average interaction energy between protein and water (Figure 7).

We tested the effects of changing the water model “in-place” by replacing the water model in the simulation trajectory, creating a 4x4 grid where the simulation trajectory

using model X was used to calculate the protein-water interaction using model Y. We found that (1) changing the water model from TIP3P→TIP3P-FB→TIP4P-EW→TIP4P-FB increased the protein-water interaction strength independent of which trajectory was used, and (2) the conformational ensembles from TIP3P→TIP3P-FB→TIP4P-EW→TIP4P-FB had increasingly strong protein-water interactions independent of which water model was used (Figure S10). Our analysis indicates that having stronger water-protein interactions *causes* proteins to become less stable, consistent with previous studies on protein-water interactions.[114]

While this is an encouraging sign of progress, we also note that all of the potentials underestimate the slope of the temperature dependence. One possible reason is that the simulated and experimental ensembles are different; the experiment is performed at constant pressure whereas the replica exchange simulations could only be done in the NVT ensemble. If the simulations had been run in the NPT ensemble instead, the density of water would have decreased at higher temperatures, which may have an effect on the helical fraction. Another possibility is the pairwise additive approximation from the force field, which neglects many-body effects such as those arising from explicit electronic polarization. Including the electronic polarizability may increase the cooperativity of helix formation and lead to a steeper temperature dependence.[117] We intend to apply this parameterization strategy and *ab initio* data set toward the parameterization of a polarizable force field in forthcoming work.

Denatured state ensemble.

A current frontier in protein simulations is the description of the denatured state ensemble (DSE), a vast conformational space where protein conformations are extended relative to the native state.[118] The DSE is closely connected with intrinsically disordered proteins,[119] which do not possess a well-defined native state and may play important roles in neurological disorders.[120] Experimentally, the average radius of gyration (R_g) of denatured proteins may be inferred from Forster resonance energy transfer (FRET) and small angle X-ray scattering (SAXS) data.[121] Simulations of the DSE have been shown to produce structures that are collapsed relative to experiment;[121] efforts to uniformly increase the strength of protein/water interactions have shown some promising results,[123] though more studies are needed to assess whether this approach applies equally well to the diverse sequences of IDPs.[124]

Here we simulated the DSE of GB3 by first denaturing the protein by running 20 ns simulations at 600 K for all 28 protein / water model combinations; we then extracted five snapshots at 1 ns intervals from the end of each trajectory, creating 140 initial structures in total with an average R_g value of 1.65 nm. We then launched 10 ns simulations for each of the 140 initial conditions for all 28 protein / water model combinations, a total of 3,960 simulations total. 2,226 of these 3,960 simulations ran to completion, representing about 800 ns of simulation time for each protein / water model combination; although 1,734 of the simulations did not run to completion, those that finished were spread as evenly as possible over the 28 protein / water model combinations. Our results are summarized in Table 4, which shows that all tested protein models systematically underestimate the

radius of gyration in comparison with experiment. Although the short simulation time of 10 ns is far from sufficient from sampling this large ensemble,[122] the calculated R_g values demonstrate some significant differences from the initial values and between the water models; for example, the TIP3P simulations predict significantly more compact distributions on average 0.2 nm smaller than TIP3P-FB. The TIP3P-FB, TIP4P-Ew and TIP4P-FB simulations produce average R_g values that are larger than the initial conditions (where $<R_g>$ = 1.65 nm), but they are all significantly less than the experimental values derived from FRET or SAXS measurements (2.2 and 2.6 nm respectively). The data indicates that the R_g values from TIP3P-FB, TIP4P-Ew, and TIP4P-FB simulations are moving in the correct direction, but longer simulations are needed to discern whether any of them are in quantitative agreement with the experimental DSE.

Conclusion

The AMBER-FB15 protein force field combines the well-established model of intermolecular interactions from AMBER94 with a systematic and thorough optimization of the intramolecular terms. The key difference in the optimized result is a significant lowering of the potential in regions away from the energy minima, which is expected to yield greater flexibility in finite temperature simulations. Our validation studies found that the predictions of equilibrium thermodynamic properties were equivalent in accuracy to published models, and the predictions of temperature dependence were significantly improved. Replacing the TIP3P water model with the updated TIP3P-FB model resulted in overall improved accuracy of the temperature dependence predictions. Our simulations of the denatured state ensemble were insufficient to conclude whether any of the models are in quantitative agreement with experiment, although the newer water models predicted larger R_g values in closer agreement with experiment compared to when TIP3P is used. Supported by the evidence in this paper, we are optimistic that the model combination AMBER-FB15/TIP3P-FB will yield accurate predictions in simulations of proteins, particularly when fluctuations away from equilibrium, conformational changes and/or temperature dependence are expected to play important roles.

Supplementary Material

Refer to Web version on PubMed Central for supplementary material.

Acknowledgements

We acknowledge Dave Case, Dave Cerutti, John Chodera and members of the Chodera Lab for insightful discussions. We acknowledge Christina Redfield for sharing the order parameter data for bacteriophage lysozyme. The simulations of protein temperature dependence were performed on the Titan supercomputer at the Oak Ridge Leadership Computing Facility (OLCF). We acknowledge Jason Swails for providing assistance with the ParmEd software package which enabled the temperature dependence simulations on Titan. The simulations of the denatured state ensemble used computational resources provided by the Open Science Grid (OSG). We acknowledge Miron Livny and the OSG Team for providing this resource and for their support. The Pande Group is broadly supported by grants from the NIH (R01 GM062868 and U19 AI109662) as well as gift funds and contributions from Folding@home donors. KAB acknowledges support from NIH grant P30CA008747, the Sloan Kettering Institute, and Starr Foundation grant I8-A8-058. THG acknowledges support from the NSF under grant CHE-1363320. TJM acknowledges support from NSF (ACI-1450179).

Bibliography

1. Bash PA; Field MJ; Davenport RC; Petsko GA; Ringe D; Karplus M, Computer Simulation and Analysis of the Reaction Pathway of Triosephosphate Isomerase. Biochemistry-Us 1991, 30 (24), 5826–5832.
2. Gao J, Catalysis by Enzyme Conformational Change as Illustrated by Orotidine 5′-Monophosphate Decarboxylase. Current Opinion in Structural Biology 2003, 13 (2), 184–192. [PubMed: 12727511]
3. Ridder L; Mulholland AJ; Rietjens IMCM; Vervoort J, A Quantum Mechanical/Molecular Mechanical Study of the Hydroxylation of Phenol and Halogenated Derivatives by Phenol Hydroxylase. J. Am. Chem. Soc. 2000, 122 (36), 8728–8738.
4. Wu N; Mo Y; Gao J; Pai EF, Electrostatic Stress in Catalysis: Structure and Mechanism of the Rnzyme Orotidine Monophosphate Decarboxylase. Proceedings of the National Academy of Sciences 2000, 97 (5), 2017–2022.
5. Jindal G; Warshel A, Exploring the Dependence of QM/MM Calculations of Enzyme Catalysis on the Size of the QM Region. J Phys Chem B 2016, 120 (37), 9913–9921. [PubMed: 27552257]
6. Casalino L; Palermo G; Rothlisberger U; Magistrato A, Who Activates the Nucleophile in Ribozyme Catalysis? An Answer from the Splicing Mechanism of Group II Introns. Journal of the American Chemical Society 2016, 138 (33), 10374–10377. [PubMed: 27309711]
7. Cortopassi WA; Kumar K; Duarte F; Pimentel AS; Paton RS, Mechanisms of Histone Lysine-modifying Enzymes: A Computational Perspective on the Role of the Protein Environment. Journal of Molecular Graphics & Modelling 2016, 67, 69–84. [PubMed: 27258188]
8. Gillet N; Ruiz-Pernia JJ; de la Lande A; Levy B; Lederer F; Demachy I; Moliner V, QM/MM study of L-lactate Oxidation by Flavocytochrome b(2). Physical Chemistry Chemical Physics 2016, 18 (23), 15609–15618. [PubMed: 27220613]
9. Roston D; Demapan D; Cui Q, Leaving Group Ability Observably Affects Transition State Structure in a Single Enzyme Active Site. Journal of the American Chemical Society 2016, 138 (23), 7386–7394. [PubMed: 27186960]
10. Samudio BM; Couch V; Stuchebrukhov AA, Monte Carlo Simulations of Glu-242 in Cytochrome c Oxidase. J Phys Chem B 2016, 120 (9), 2095–2105. [PubMed: 26865374]
11. Ferrara P; Apostolakis J; Caflisch A, Thermodynamics and Kinetics of Folding of Two Model Peptides Investigated by Molecular Dynamics Simulations. The Journal of Physical Chemistry B 2000, 104 (20), 5000–5010.
12. Leopold PE; Montal M; Onuchic JN, Protein Folding Funnels: A Kinetic Approach to the Sequence-Structure Relationship. Proceedings of the National Academy of Sciences 1992, 89 (18), 8721–8725.
13. Onuchic JN; Socci ND; Luthey-Schulten Z; Wolynes PG, Protein Folding Funnels: The Nature of the Transition State Ensemble. Folding and Design 1996, 1 (6), 441–450. [PubMed: 9080190]
14. Šali A; Shakhnovich E; Karplus M, How Does a Protein Fold? Nature 1994, 369 (6477), 248–251. [PubMed: 7710478]
15. Šali A; Shakhnovich E; Karplus M, Kinetics of Protein Folding. Journal of Molecular Biology 1994, 235 (5), 1614–1636. [PubMed: 8107095]
16. Snow CD; Nguyen N; Pande VS; Gruebele M, Absolute Comparison of Simulated and Experimental Protein-folding Dynamics. Nature 2002, 420 (6911), 102–106. [PubMed: 12422224]
17. Dill KA; Ozkan SB; Shell MS; Weikl TR, The Protein Folding Problem. In Annual Review of Biophysics, 2008; Vol. 37, pp 289–316.
18. Shea JE; Brooks CL, From Folding Theories to Folding Proteins: A Review and Assessment of Simulation Studies of Protein Folding and Unfolding. Annual Review of Physical Chemistry 2001, 52, 499–535.
19. Gallicchio E; Levy RM, Recent Theoretical and Computational Advances for Modeling Protein–Ligand Binding Affinities. In Computational chemistry methods in structural biology, Elsevier BV: 2011; pp 27–80.
20. Jorgensen WL, The Many Roles of Computation in Drug Discovery. Science 2004, 303 (5665), 1813–1818. [PubMed: 15031495]

21. Marelius J; Hansson T; Åqvist J, Calculation of Ligand Binding Free Energies from Molecular Dynamics Simulations. Int. J. Quant. Chem 1998, 69 (1), 77–88.
22. Wereszczynski J; McCammon JA, Statistical Mechanics and Molecular Dynamics in Evaluating Thermodynamic Properties of Biomolecular Recognition. Quarterly Reviews of Biophysics 2011, 45 (01), 1–25. [PubMed: 22082669]
23. Gilson MK; Zhou HX, Calculation of Protein-Ligand Binding Affinities. In Annual Review of Biophysics and Biomolecular Structure, 2007; Vol. 36, pp 21–42.
24. Grubmuller H; Heymann B; Tavan P, Ligand Binding: Molecular Mechanics Calculation of the Streptavidin Biotin Rupture Force. Science 1996, 271 (5251), 997–999. [PubMed: 8584939]
25. Isralewitz B; Gao M; Schulten K, Steered Molecular Dynamics and Mechanical Functions of Proteins. Current Opinion in Structural Biology 2001, 11 (2), 224–230. [PubMed: 11297932]
26. Sherman W; Day T; Jacobson MP; Friesner RA; Farid R, Novel Procedure for Modeling Ligand/Receptor Induced Fit Effects. Journal of Medicinal Chemistry 2006, 49 (2), 534–553. [PubMed: 16420040]
27. Böckmann RA; Grubmüller H, Nanoseconds Molecular Dynamics Simulation of Primary Mechanical Energy Transfer Steps in F1-ATP Synthase. Nature Structural Biology 2002, 9 (198-202).
28. Kruger P, Extending the Capabilities of Targeted Molecular Dynamics: Simulation of a Large Conformational Transition in Plasminogen Activator Inhibitor 1. Protein Science 2001, 10 (4), 798–808. [PubMed: 11274471]
29. Ma J; Sigler PB; Xu Z; Karplus M, A Dynamic Model for the Allosteric Mechanism of GroEL. Journal of Molecular Biology 2000, 302 (2), 303–313. [PubMed: 10970735]
30. Yang W; Gao YQ; Cui Q; Ma J; Karplus M, The Missing Link Between Thermodynamics and Structure in F1-ATPase. Proceedings of the National Academy of Sciences 2003, 100 (3), 874–879.
31. Shukla D; Meng YL; Roux B; Pande VS, Activation Pathway of Src Kinase Reveals Intermediate States as Targets for Drug Design. Nature Communications 2014, 5, 3397.
32. Onufriev A; Bashford D; Case DA, Exploring Protein Native States and Large-scale Conformational Changes with a Modified Generalized Born Model. Proteins-Structure Function and Bioinformatics 2004, 55 (2), 383–394.
33. Splettstoesser T; Holmes KC; Noe F; Smith JC, Structural Modeling and Molecular Dynamics Simulation of the Actin Filament. Proteins-Structure Function and Bioinformatics 2011, 79 (7), 2033–2043.
34. Kulik HJ; Luehr N; Ufimtsev IS; Martinez TJ, Ab Initio Quantum Chemistry for Protein Structures. The Journal of Physical Chemistry B 2012, 116 (41), 12501–12509. [PubMed: 22974088]
35. Rudberg E; Rubensson EH; Sałek P, Hartree–Fock Calculations with Linearly Scaling Memory Usage. The Journal of Chemical Physics 2008, 128 (18), 184106. [PubMed: 18532798]
36. Ufimtsev IS; Luehr N; Martinez TJ, Charge Transfer and Polarization in Solvated Proteins from Ab Initio Molecular Dynamics. J. Phys. Chem. Lett 2011, 2 (14), 1789–1793.
37. Lifson S, Consistent Force Field for Calculations of Conformations, Vibrational Spectra, and Enthalpies of Cycloalkane and n-Alkane Molecules. The Journal of Chemical Physics 1968, 49 (11), 5116.
38. Levitt M; Lifson S, Refinement of Protein Conformations using a Macromolecular Energy Minimization Procedure. Journal of Molecular Biology 1969, 46 (2), 269–279. [PubMed: 5360040]
39. Jorgensen WL; Tirado-Rives J, The OPLS [Optimized Potentials for Liquid Simulations] Potential Functions for Proteins, Energy Minimizations for Crystals of Cyclic Peptides and Crambin. Journal of the American Chemical Society 1988, 110 (6), 1657–1666. [PubMed: 27557051]
40. Brooks BR; Bruccoleri RE; Olafson BD; States DJ; Swaminathan S; Karplus M, Charmm - A Program For Macromolecular Energy, Minimization, And Dynamics Calculations. Journal of Computational Chemistry 1983, 4 (2), 187–217.

41. MacKerell AD; Bashford D; Bellott M; Dunbrack RL; Evanseck JD; Field MJ; Fischer S; Gao J; Guo H; Ha S; et al. , All-atom Empirical Potential for Molecular Modeling and Dynamics Studies of Proteins. J Phys Chem B 1998, 102 (18), 3586–3616. [PubMed: 24889800]

42. Mackerell AD; Feig M; Brooks CL, Extending the Treatment of Backbone Energetics in Protein Force Fields: Limitations of Gas-Phase Quantum Mechanics in Reproducing Protein Conformational Distributions in Molecular Dynamics Simulations. Journal of Computational Chemistry 2004, 25 (11), 1400–1415. [PubMed: 15185334]

43. Huang J; MacKerell AD, CHARMM36 All-Atom Additive Protein Force Field: Validation Based on Comparison to NMR Data. Journal of Computational Chemistry 2013, 34 (25), 2135–2145. [PubMed: 23832629]

44. Lopes PEM; Guvench O; MacKerell AD, Current Status of Protein Force Fields for Molecular Dynamics Simulations. In Molecular Modeling of Proteins: 2nd Edition, Kukol A, Ed. 2015; Vol. 1215, pp 47–71.

45. Ponder JW; Case DA, Force Fields for Protein Simulations. Protein Simulations 2003, 66, 27–85.

46. Mackerell AD, Empirical Force Fields for Biological Macromolecules: Overview and Issues. Journal of Computational Chemistry 2004, 25 (13), 1584–1604. [PubMed: 15264253]

47. Wang W; Donini O; Reyes CM; Kollman PA, Biomolecular Simulations: Recent Developments in Force Fields, Simulations of Enzyme Catalysis, Protein-Ligand, Protein-Protein, and Protein-Nucleic Acid Noncovalent Interactions. Annual Review of Biophysics and Biomolecular Structure 2001, 30, 211–243.

48. Cornell WD; Cieplak P; Bayly CI; Gould IR; Merz KM; Ferguson DM; Spellmeyer DC; Fox T; Caldwell JW; Kollman PA, A Second Generation Force Field for the Simulation of Proteins, Nucleic Acids, and Organic Molecules. J. Am. Chem. Soc 1995, 117 (19), 5179–5197.

49. Bayly CI; Cieplak P; Cornell W; Kollman PA, A Well-behaved Electrostatic Potential Based Method using Charge Restraints for Deriving Atomic Charges: The RESP Model. The Journal of Physical Chemistry 1993, 97 (40), 10269–10280.

50. Jakalian A; Bush BL; Jack DB; Bayly CI, Fast, Efficient Generation of High-Quality Atomic Charges. AM1-BCC model: I. Method. Journal of Computational Chemistry 2000, 21 (2), 132–146.

51. Jakalian A; Jack DB; Bayly CI, Fast, Efficient Generation of High-Quality Atomic Charges. AM1-BCC model: II. Parameterization and Validation. Journal of Computational Chemistry 2002, 23 (16), 1623–1641. [PubMed: 12395429]

52. Wang J; Cieplak P; Kollman PA, How Well Does a Restrained Electrostatic Potential (RESP) Model Perform in Calculating Conformational Energies of Organic and Biological Molecules? Journal of Computational Chemistry 2000, 21 (12), 1049–1074.

53. Hornak V; Abel R; Okur A; Strockbine B; Roitberg A; Simmerling C, Comparison of Multiple Amber Force Fields and Development of Improved Protein Backbone Parameters. Proteins: Structure, Function, and Bioinformatics 2006, 65 (3), 712–725.

54. Garcia AE; Sanbonmatsu KY, Helical Stabilization by Side Chain Shielding of Backbone Hydrogen Bonds. Proceedings of the National Academy of Sciences 2002, 99 (5), 2782–2787.

55. Lindorff-Larsen K; Piana S; Palmo K; Maragakis P; Klepeis JL; Dror RO; Shaw DE, Improved Side-Chain Torsion Potentials for the Amber ff99SB Protein Force Field. Proteins: Structure, Function, and Bioinformatics 2010, 78 (8), 1950–1958.

56. Feyereisen M; Fitzgerald G; Komornicki A, Use Of Approximate Integrals In Abinitio Theory - An Application In MP2 Energy Calculations. Chemical Physics Letters 1993, 208 (5-6), 359–363.

57. Distasio RA; Steele RP; Rhee YM; Shao YH; Head-Gordon M, An Improved Algorithm for Analytical Gradient Evaluation in Resolution-of-the-Identity Second-Order Moller-Plesset Perturbation Theory: Application to Alanine Tetrapeptide Conformational Analysis. Journal of Computational Chemistry 2007, 28 (5), 839–856. [PubMed: 17219361]

58. Kendall RA; Dunning TH; Harrison RJ, Electron-Affinities Of The 1st-Row Atoms Revisited - Systematic Basis-Sets And Wave-Functions. J Chem Phys 1992, 96 (9), 6796–6806.

59. Li DW; Bruschweiler R, NMR-Based Protein Potentials. Angewandte Chemie-International Edition 2010, 49 (38), 6778–6780. [PubMed: 20715028]

60. Shaw DE; Maragakis P; Lindorff-Larsen K; Piana S; Dror RO; Eastwood MP; Bank JA; Jumper JM; Salmon JK; Shan Y; Wriggers W, Atomic-Level Characterization of the Structural Dynamics of Proteins. Science 2010, 330 (6002), 341–346. [PubMed: 20947758]
61. Cerutti DS; Rice JE; Swope WC; Case DA, Derivation of Fixed Partial Charges for Amino Acids Accommodating a Specific Water Model and Implicit Polarization. J Phys Chem B 2013, 117 (8), 2328–2338. [PubMed: 23379664]
62. Debiec KT; Cerutti DS; Baker LR; Gronenborn AM; Case DA; Chong LT, Further along the Road Less Traveled: AMBER ff15ipq, an Original Protein Force Field Built on a Self-Consistent Physical Model. J. Chem. Theory Comput 2016, 12 (8), 3926–3947. [PubMed: 27399642]
63. Lopes PEM; Huang J; Shim J; Luo Y; Li H; Roux B; MacKerell AD, Polarizable Force Field for Peptides and Proteins Based on the Classical Drude Oscillator. J. Chem. Theory Comput 2013, 9 (12), 5430–5449. [PubMed: 24459460]
64. Shi Y; Xia Z; Zhang J; Best R; Wu C; Ponder JW; Ren P, Polarizable Atomic Multipole-Based AMOEBA Force Field for Proteins. J. Chem. Theory Comput. 2013, 9 (9), 4046–4063. [PubMed: 24163642]
65. Wang L-P; Martinez TJ; Pande VS, Building Force Fields: An Automatic, Systematic, and Reproducible Approach. J. Phys. Chem. Lett 2014, 5 (11), 1885–1891. [PubMed: 26273869]
66. Horn HW; Swope WC; Pitera JW; Madura JD; Dick TJ; Hura GL; Head-Gordon T, Development of an Improved Four-Site Water Model for Biomolecular Simulations: TIP4P-Ew. J Chem Phys 2004, 120 (20), 9665–9678. [PubMed: 15267980]
67. Darden T; York D; Pedersen L, Particle Mesh Ewald - An N.Log(N) Method For Ewald Sums In Large Systems. J Chem Phys 1993, 98 (12), 10089–10092.
68. Wang L-P ForceBalance code and data repository on GitHub. https://github.com/leeping/forcebalance (accessed 2016/11/03).
69. Helgaker T; Klopper W; Koch H; Noga J, Basis-Set Convergence of Correlated Calculations on Water. J Chem Phys 1997, 106 (23), 9639–9646.
70. Merrick JP; Moran D; Radom L, An Evaluation of Harmonic Vibrational Frequency Scale Factors. Journal of Physical Chemistry A 2007, 111 (45), 11683–11700. [PubMed: 17948971]
71. Wang L-P; Chen J; Van Voorhis T, Systematic Parametrization of Polarizable Force Fields from Quantum Chemistry Data. J. Chem. Theory Comput 2013, 9 (1), 452–460. [PubMed: 26589047]
72. Wang L-P; Head-Gordon T; Ponder JW; Ren P; Chodera JD; Eastman PK; Martinez TJ; Pande VS, Systematic Improvement of a Classical Molecular Model of Water. The Journal of Physical Chemistry B 2013, 117 (34), 9956–9972. [PubMed: 23750713]
73. Zhou CY; Jiang F; Wu YD, Residue-Specific Force Field Based on Protein Coil Library. RSFF2: Modification of AMBER ff99SB. J Phys Chem B 2015, 119 (3), 1035–1047. [PubMed: 25358113]
74. Maier JA; Martinez C; Kasavajhala K; Wickstrom L; Hauser KE; Simmerling C, ff14SB: Improving the Accuracy of Protein Side Chain and Backbone Parameters from ff99SB. Journal of Chemical Theory and Computation 2015, 11 (8), 3696–3713. [PubMed: 26574453]
75. Dennis JE; Gay DM; Walsh RE, An Adaptive Nonlinear Least-Squares Algorithm. ACM Transactions on Mathematical Software 1981, 7 (3), 348–368.
76. Marquardt DW, An Algorithm for Least-Squares Estimation of Nonlinear Parameters. Journal of the Society for Industrial and Applied Mathematics 1963, 11 (2), 431–441.
77. Moré JJ, The Levenberg-Marquardt Algorithm: Implementation and Theory. In Lecture Notes in Mathematics, Springer Nature: 1978; pp 105–116.
78. Moré JJ; Sorensen DC, Computing a Trust Region Step. SIAM Journal on Scientific and Statistical Computing 1983, 4 (3), 553–572.
79. Jones E; Oliphant T; Peterson P; others SciPy: Open Source Scientific Tools for Python. http://www.scipy.org/ (accessed 2016/11/11).
80. Ponder JW TINKER: Software Tools for Molecular Design. (accessed 2016/10/22).
81. Krylov AI; Gill PMW, Q-Chem: an engine for innovation. Wiley Interdisciplinary Reviews: Computational Molecular Science 2012, 3 (3), 317–326.

82. Shao Y; Gan Z; Epifanovsky E; Gilbert ATB; Wormit M; Kussmann J; Lange AW; Behn A; Deng J; Feng X; et al. , Advances in Molecular Quantum Chemistry Contained in the Q-Chem 4 Program Package. Molecular Physics 2015, 113 (2), 184–215.
83. Albrecht M; Rajan D; Thain D, Making Work Queue Cluster-Friendly for Data Intensive Scientific Applications. In 2013 IEEE International Conference on Cluster Computing (CLUSTER), Institute of Electrical and Electronics Engineers (IEEE): 2013.
84. Turney JM; Simmonett AC; Parrish RM; Hohenstein EG; Evangelista FA; Fermann JT; Mintz BJ; Burns LA; Wilke JJ; Abrams ML; et al. , Psi4: An Open-Source Ab Initio Electronic Structure Program. Wiley Interdisciplinary Reviews: Computational Molecular Science 2011, 2 (4), 556–565.
85. Abraham MJ; Murtola T; Schulz R; Páll S; Smith JC; Hess B; Lindahl E, GROMACS: High Performance Molecular Simulations through Multi-Level Parallelism from Laptops to Supercomputers. SoftwareX 2015, 1-2, 19–25.
86. McGibbon RT; Beauchamp KA; Harrigan MP; Klein C; Swails Jason M.; Hernández CX; Schwantes CR; Wang L-P; Lane TJ; Pande VS, MDTraj: A Modern Open Library for the Analysis of Molecular Dynamics Trajectories. Biophysical Journal 2015, 109 (8), 1528–1532. [PubMed: 26488642]
87. Han B; Liu YF; Ginzinger SW; Wishart DS, SHIFTX2: Significantly Improved Protein Chemical Shift Prediction. Journal of Biomolecular Nmr 2011, 50 (1), 43–57. [PubMed: 21448735]
88. Swails JM; Hernandez CX; Mobley DL; Nguyen H; Wang L-P; Janowski P ParmEd: Cross-Program Parameter and Topology File Editor and Molecular Mechanical Simulator Engine. https://github.com/ParmEd/ParmEd (accessed 2016/11/11).
89. Salomon-Ferrer R; Case DA; Walker RC, An Overview of the Amber Biomolecular Simulation Package. Wiley Interdisciplinary Reviews-Computational Molecular Science 2013, 3 (2), 198–210.
90. Roe DR; Cheatham TE, PTRAJ and CPPTRAJ: Software for Processing and Analysis of Molecular Dynamics Trajectory Data. Journal of Chemical Theory and Computation 2013, 9 (7), 3084–3095. [PubMed: 26583988]
91. McGibbon RT; Beauchamp KA; Harrigan MP; Klein C; Swails JM; Hernandez CX; Schwantes CR; Wang LP; Lane TJ; Pande VS, MDTraj: A Modern Open Library for the Analysis of Molecular Dynamics Trajectories. Biophysical Journal 2015, 109 (8), 1528–1532. [PubMed: 26488642]
92. Altunay M; Avery P; Blackburn K; Bockelman B; Ernst M; Fraser D; Quick R; Gardner R; Goasguen S; Levshina T; et al. , A Science Driven Production Cyberinfrastructure-the Open Science Grid. Journal of Grid Computing 2011, 9 (2), 201–218.
93. Aqvist J, Ion Water Interaction Potentials Derived From Free-Energy Perturbation Simulations. Journal of Physical Chemistry 1990, 94 (21), 8021–8024.
94. Anandakrishnan R; Aguilar B; Onufriev AV, H++3.0: Automating pK Prediction and the Preparation of Biomolecular Structures for Atomistic Molecular Modeling and Simulations. Nucleic Acids Research 2012, 40 (W1), W537–W541. [PubMed: 22570416]
95. Koller AN; Schwalbe H; Gohlke H, Starting Structure Dependence of NMR Order Parameters Derived from MD Simulations: Implications for Judging Force-Field Quality. Biophysical Journal 2008, 95 (1), L4–L6.
96. Prompers JJ; Bruschweiler R, General Framework for Studying the Dynamics of Folded and Nonfolded Proteins by NMR Relaxation Spectroscopy and MD Simulation. Journal of the American Chemical Society 2002, 124 (16), 4522–4534. [PubMed: 11960483]
97. Smith LJ; Bowen AM; Di Paolo A; Matagne A; Redfield C, The Dynamics of Lysozyme from Bacteriophage Lambda in Solution Probed by NMR and MD Simulations. Chembiochem 2013, 14 (14), 1780–1788. [PubMed: 23801644]
98. Smith LJ; van Gunsteren WF; Hansen N, Characterization of the Flexible Lip Regions in Bacteriophage Lambda Lysozyme using MD Simulations. Eur. Biophys. J. Biophys. Lett 2015, 44 (4), 235–247.
99. Case DA, Interpretation of Chemical Shifts and Coupling Constants in Macromolecules. Current Opinion in Structural Biology 2000, 10 (2), 197–203. [PubMed: 10753812]

100. Case DA; Scheurer C; Bruschweiler R, Static and dynamic effects on vicinal scalar J couplings in proteins and peptides: A MD/DFT analysis. Journal of the American Chemical Society 2000, 122 (42), 10390–10397.

101. Perez C; Lohr F; Ruterjans H; Schmidt JM, Self-Consistent Karplus Parametrization of (3)J Couplings Depending on the Polypeptide Side-Chain Torsion Chi(1). Journal of the American Chemical Society 2001, 123 (29), 7081–7093. [PubMed: 11459487]

102. Schmidt JM; Blumel M; Lohr F; Ruterjans H, Self-Consistent (3)J Coupling Analysis for the Joint Calibration of Karplus Coefficients and Evaluation of Torsion Angles. Journal of Biomolecular Nmr 1999, 14 (1), 1–12. [PubMed: 21136331]

103. Vuister GW; Bax A, Quantitative J Correlation - A New Approach For Measuring Homonuclear 3-Bond J(H(N)H(Alpha) Coupling-Constants In N-15-Enriched Proteins. Journal of the American Chemical Society 1993, 115 (17), 7772–7777.

104. Vuister GW; Wang AC; Bax A, Measurement Of 3-Bond Nitrogen Carbon-J Couplings In Proteins Uniformly Enriched In N-15 And C-13. Journal of the American Chemical Society 1993, 115 (12), 5334–5335.

105. Best RB; Hummer G, Optimized Molecular Dynamics Force Fields Applied to the Helix-Coil Transition of Polypeptides. J Phys Chem B 2009, 113 (26), 9004–9015. [PubMed: 19514729]

106. Shalongo W; Dugad L; Stellwagen E, Distribution Of Helicity Within The Model Peptide Acetyl(AAQAA)(3)Amide. Journal of the American Chemical Society 1994, 116 (18), 8288–8293.

107. Davis CM; Xiao SF; Raeigh DP; Dyer RB, Raising the Speed Limit for beta-Hairpin Formation. Journal of the American Chemical Society 2012, 134 (35), 14476–14482. [PubMed: 22873643]

108. Case DA; Cheatham TE; Darden T; Gohlke H; Luo R; Merz KM; Onufriev A; Simmerling C; Wang B; Woods RJ, The Amber Biomolecular Simulation Programs. Journal of Computational Chemistry 2005, 26 (16), 1668–1688. [PubMed: 16200636]

109. Pitera JW; Swope W, Understanding Folding and Design: Replica-Exchange Simulations of "Trp-cage" Fly Miniproteins. P Natl Acad Sci USA 2003, 100 (13), 7587–7592.

110. Pang Y-P, FF12MC: A Revised AMBER Forcefield and New Protein Simulation Protocol. Proteins: Structure, Function, and Bioinformatics 2016, 84 (10), 1490–1516.

111. Harder E; Damm W; Maple J; Wu CJ; Reboul M; Xiang JY; Wang LL; Lupyan D; Dahlgren MK; Knight JL; et al. , OPLS3: A Force Field Providing Broad Coverage of Drug-like Small Molecules and Proteins. Journal of Chemical Theory and Computation 2016, 12 (1), 281–296. [PubMed: 26584231]

112. Piana S; Lindorff-Larsen K; Shaw DE, How Robust Are Protein Folding Simulations with Respect to Force Field Parameterization? Biophysical Journal 2011, 100 (9), L47–L49. [PubMed: 21539772]

113. Lindorff-Larsen K; Maragakis P; Piana S; Eastwood MP; Dror RO; Shaw DE, Systematic Validation of Protein Force Fields against Experimental Data. Plos One 2012, 7 (2), e32131. [PubMed: 22384157]

114. Nerenberg PS; Head-Gordon T, Optimizing Protein-Solvent Force Fields to Reproduce Intrinsic Conformational Preferences of Model Peptides. Journal of Chemical Theory and Computation 2011, 7 (4), 1220–1230. [PubMed: 26606367]

115. Nerenberg PS; Jo B; So C; Tripathy A; Head-Gordon T, Optimizing Solute-Water van der Waals Interactions to Reproduce Solvation Free Energies. J Phys Chem B 2012, 116, 4524–4534. [PubMed: 22443635]

116. Zhou AQ; O'Hern CS; Regan L, Predicting the Side-Chain Dihedral Angle Distributions of Nonpolar, Aromatic, and Polar Amino Acids using Hard Sphere Models. Proteins-Structure Function and Bioinformatics 2014, 82 (10), 2574–2584.

117. Lemkul JA; Huang J; Roux B; MacKerell AD, An Empirical Polarizable Force Field Based on the Classical Drude Oscillator Model: Development History and Recent Applications. Chemical Reviews 2016, 116 (9), 4983–5013. [PubMed: 26815602]

118. Tompa P, Unstructural Biology Coming of Age. Current Opinion in Structural Biology 2011, 21 (3), 419–425. [PubMed: 21514142]

119. Fawzi NL; Phillips AH; Ruscio JZ; Doucleff M; Wemmer DE; Head-Gordon T, Structure and Dynamics of the Abeta(21-30) Peptide from the Interplay of NMR Experiments and Molecular Simulations. J Am Chem Soc 2008, 130 (19), 6145–58. [PubMed: 18412346]

120. Uversky VN; Oldfield CJ; Dunker AK, Intrinsically Disordered Proteins in Human Diseases: Introducing the D(2) Concept. In Annual Review of Biophysics, 2008; Vol. 37, pp 215–246.

121. Skinner JJ; Yu W; Gichana EK; Baxa MC; Hinshaw JR; Freed KF; Sosnick TR, Benchmarking All-Atom Simulations using Hydrogen Exchange. P Natl Acad Sci USA 2014, 111 (45), 15975–15980.

122. Lindorff-Larsen K; Trbovic N; Maragakis P; Piana S; Shaw DE, Structure and Dynamics of an Unfolded Protein Examined by Molecular Dynamics Simulation. Journal of the American Chemical Society 2012, 134 (8), 3787–3791. [PubMed: 22339051]

123. Piana S; Donchev AG; Robustelli P; Shaw DE, Water Dispersion Interactions Strongly Influence Simulated Structural Properties of Disordered Protein States. J Phys Chem B 2015, 119 (16), 5113–5123. [PubMed: 25764013]

124. Henriques J; Skepo M, Molecular Dynamics Simulations of Intrinsically Disordered Proteins: On the Accuracy of the TIP4P-D Water Model and the Representativeness of Protein Disorder Models. Journal of Chemical Theory and Computation 2016, 12 (7), 3407–3415. [PubMed: 27243806]

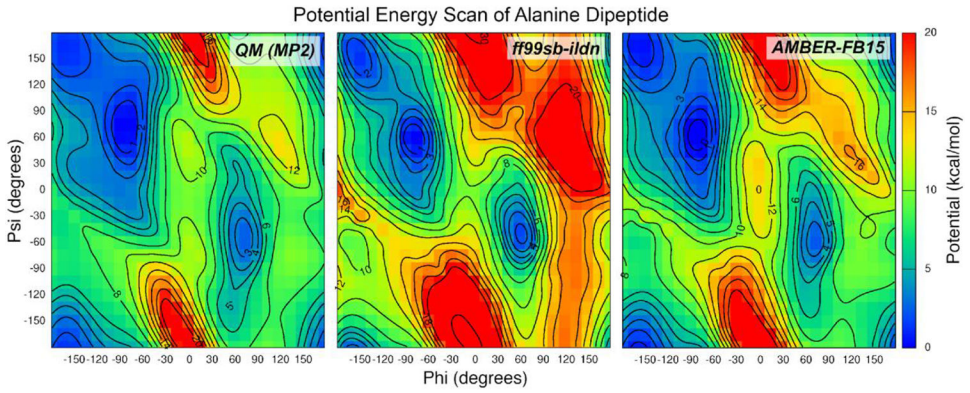

Figure 1.

Plot of the potential energy in alanine dipeptide calculated for energy-minimized structures at the MP2/aug-cc-pVTZ level with the (φ,ψ) dihedral angles constrained. Color indicates the relative potential energy with respect to the minimum.

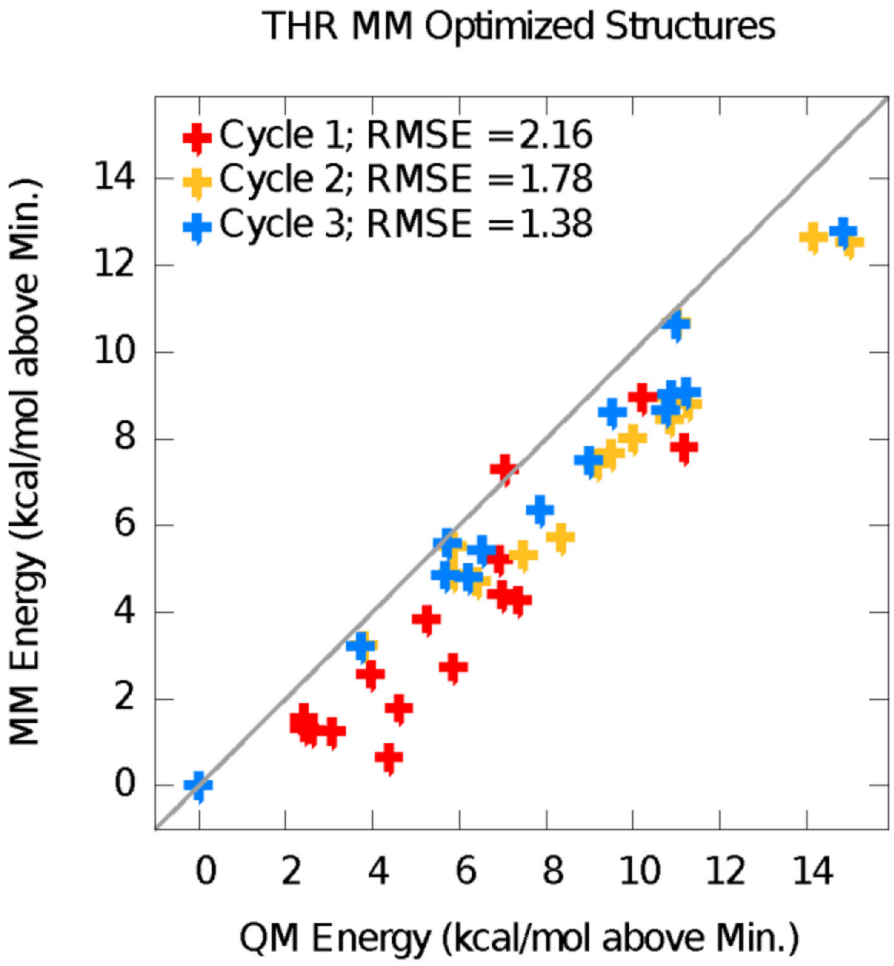

Figure 2.

MM vs. QM potential energies for MM-optimized geometries of threonine dipeptide. Each data point corresponds to a local energy minimum predicted by the force field. The Cycle 1 parameters were fitted to QM data from the torsion scans only. The QM data points at the local minima of Cycle 1 are added to the optimization of the Cycle 2 parameters. Cycle 3 is the final parameter set. The spurious MM energy minima (points far below the diagonal line) are eliminated in later cycles.

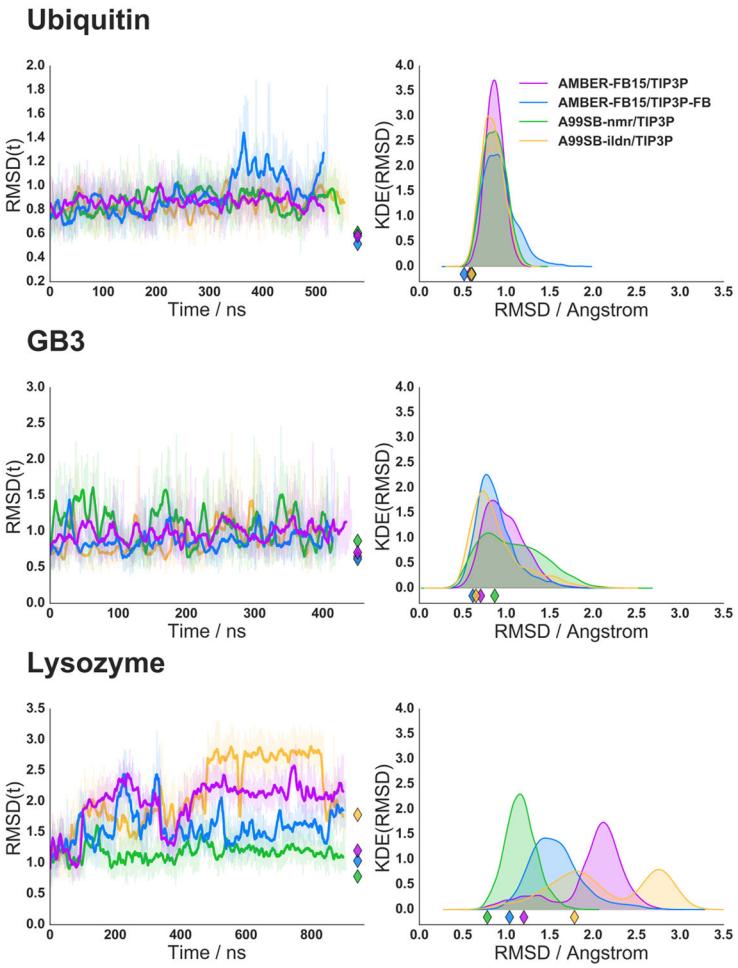

Figure 3.

Time series of RMSD to the experimental crystal structure for three proteins and four simulations. The right panels show Gaussian kernel density estimates of the RMSD values. The diamond markers indicate the RMSD to the crystal structure using the Cartesian-averaged protein backbone conformations over the whole simulation.

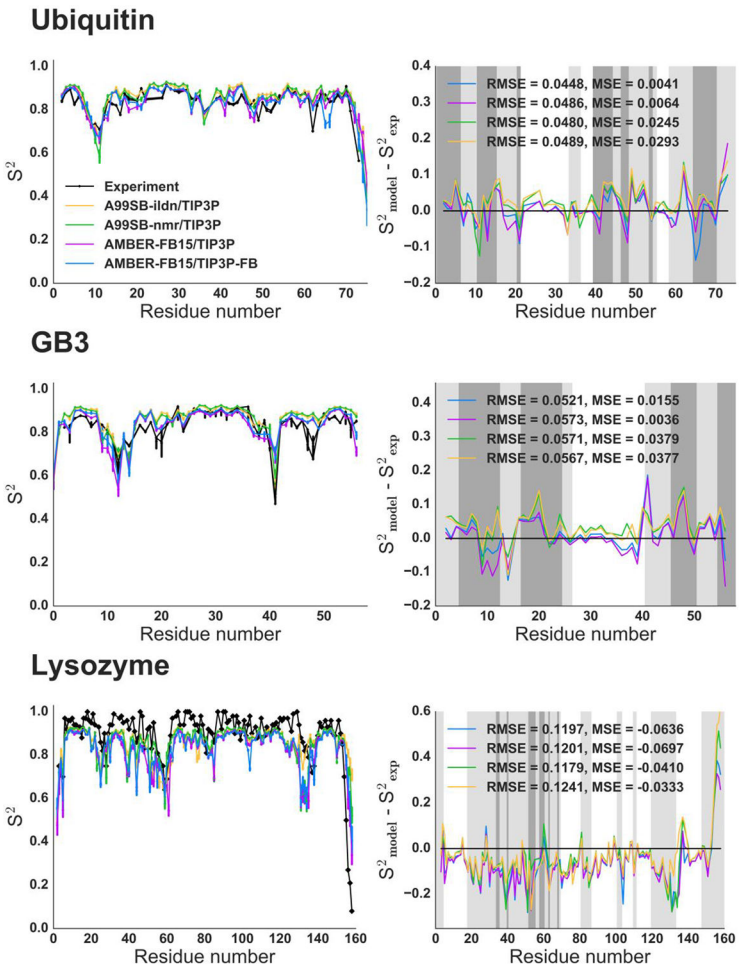

Figure 4.

Lipari-Szabo S^2 order parameters and error residuals compared to experimental NMR measurements. The root-mean-squared error (RMSE) and mean signed error (MSE) of the simulated observables with respect to experiment are given in the legends. The background of the error residual plots are colored according to secondary structure as determined by DSSP analysis (white, helix; light gray, coil; dark gray, strand).

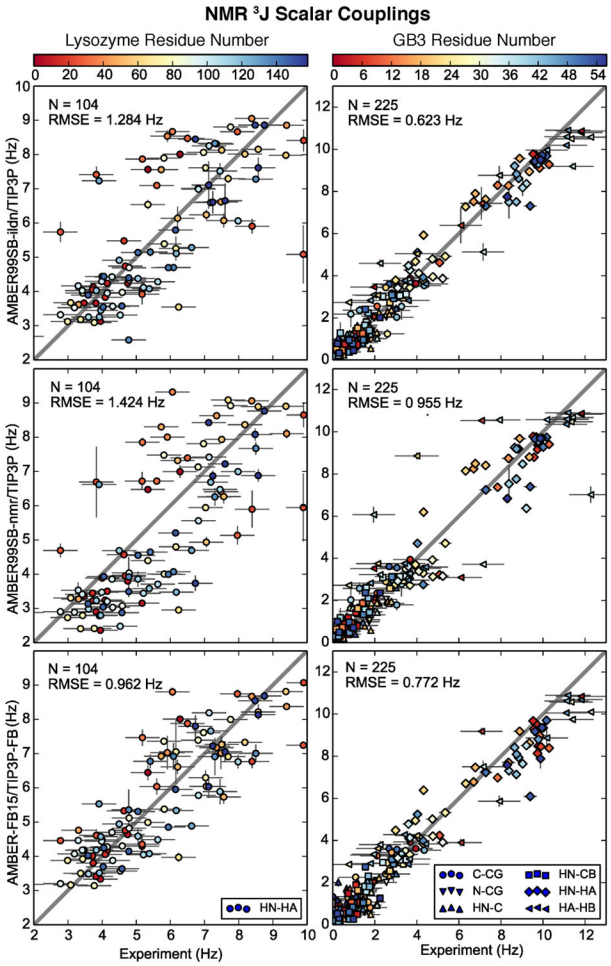

Figure 5.

Scatter plots of experimental vs. calculated NMR three-bond scalar couplings. Two proteins are shown (left: bacteriophage lysozyme, PDB ID 1AM7, right: GB3, PDB ID 1IGD) and three models (top, AMBER99SB-ildn/TIP3P; middle, AMBER99SB-nmr/TIP3P; bottom, AMBER-FB15/TIP3P-FB from this work.) Symbols represent the atom pair involved in the coupling, and colors represent the position of the residue in the protein sequence.

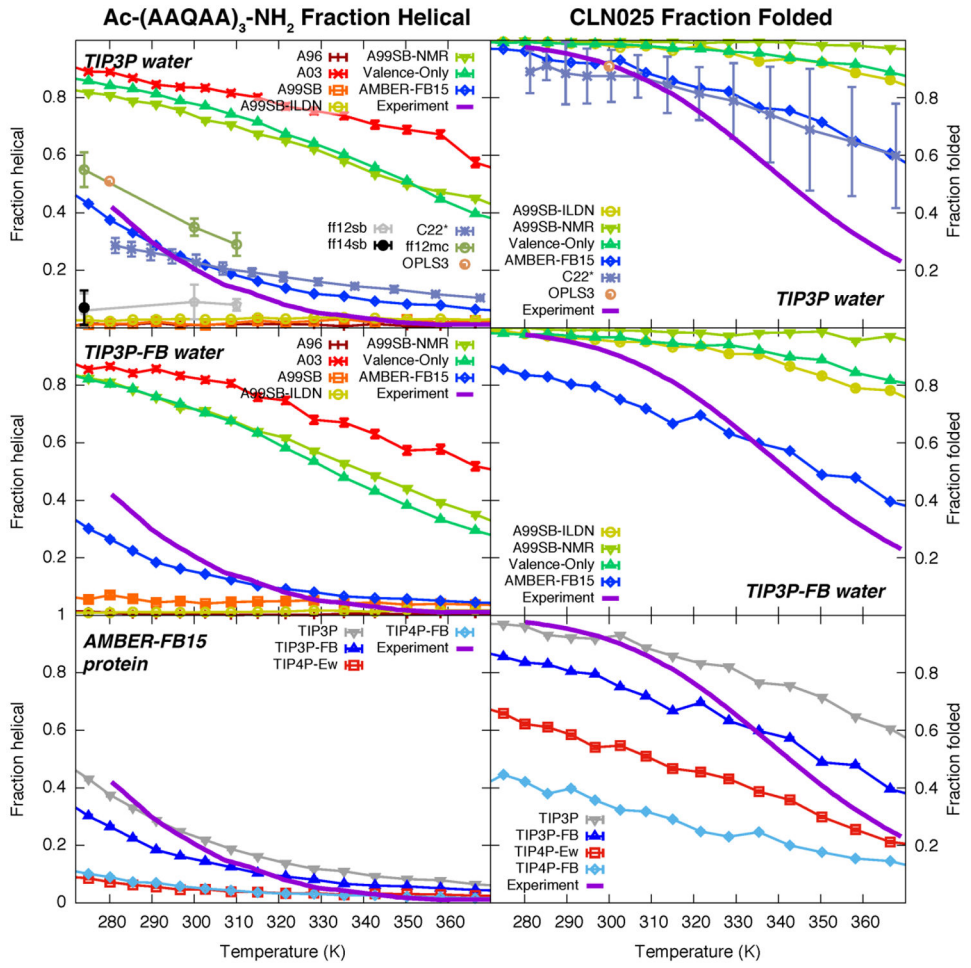

Figure 6.

Temperature dependence of secondary structure for two small peptides as a function of temperature and several force field / water model combinations. The performance of the AMBER-FB15 / TIP3P-FB model combination is the dark blue trace in the middle row. Left column: The helical fraction of Ac-$(AAQAA)_3$-NH_2. Right column: The fraction folded of CLN025. Top row: Comparison of multiple protein force fields using TIP3P water model. Middle row: Same comparison using TIP3P-FB water model. Bottom row: Comparison of four water models using AMBER-FB15 protein force field.

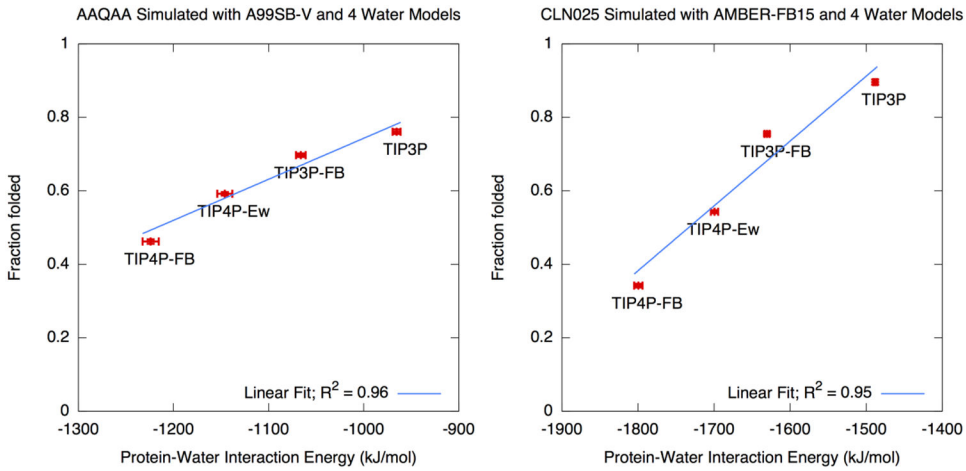

Figure 7.

Correlation between average protein-water interaction energy and fraction of secondary structure. Left: AAQAA simulated with A99SB-V (left). Right: CLN025 simulated with AMBER-FB15 (right). Each plot contains four simulations with four water models. Error bars represent one standard error.

Table 1.

Types of parameterization data for AMBER-FB15 force field.

Reference Data	**# Calcs.**
Energy, gradients of 26 amino acids over (φ, ψ) (incl. ASH, CYM, GLH, HIE, HIP, LYN)	14,971
Energy, gradients of 21 amino acids over (χ_1, χ_2) (excluding ALA, CYM, GLY, PRO, VAL)	12,093
Energy, gradients of CYM, VAL over (φ, χ_1)	1,151
Vibrational frequencies and eigenvectors for 20 amino acids	20
Energy, gradients of MM-optimized structures	1,060

Table 2.

Prior width values for each parameter type.

Parameter Type	Prior Width
Bond length	0.01 nm
Bond force constant	10^5 kJ mol^{-1} nm^{-2}
Bond angle	5°
Angle force constant	100 kJ mol^{-1} rad^{-2}
Dihedral phase	π rad
Dihedral amplitude	10 kJ mol^{-1}

Table 3.

Optimized objective function (χ^2) values in a preliminary run of ForceBalance using only the energies from the first two rows of Table 1. The results indicate that all parameter types have a significant impact on lowering the objective function.

Model	Bond	Angle	Dihedrals	Side Chains	*N* (Params)	MUE (kcal/mol)	Objective Function χ^2
	Initial Parameters (A99SB)					2.78	38.0
Prelim 1	No	No	k_φ	No	69	1.69	16.8
Prelim 2	No	No	k_φ, φ_0	No	138	1.65	12.6
Prelim 3	k_b	k_θ	k_φ	No	210	1.34	11.9
A99SB-V	k_b, b_0	k_θ, θ_0	k_φ, φ_0	No	420	1.00	6.0
AMBER-FB15	k_b, b_0	k_θ, θ_0	k_φ, φ_0	k_φ, φ_0	1406	0.80	4.1

Table 4.

Average radius of gyration (R_g) of the denatured state ensemble of GB3 simulated using seven protein models and four water models, started from an ensemble of initial conditions with an average R_g value of 1.65 nm. Bold entries denote average R_g values in excess of 1.9 nm. The experimental measurements are 2.2 nm (FRET) and 2.6 nm (SAXS) from Ref. 121.

	TIP3P	TIP3P-FB	TIP4P-EW	TIP4P-FB
A96	1.80 (0.10)	**1.99 (0.16)**	**1.92 (0.10)**	1.88 (0.08)
A03	1.42 (0.06)	1.77 (0.15)	1.65 (0.08)	1.79 (0.12)
A99SB	1.69 (0.11)	1.83 (0.14)	1.75 (0.09)	1.84 (0.11)
A99SB-ILDN	1.70 (0.13)	1.77 (0.12)	1.82 (0.11)	**2.01 (0.11)**
A99SB-NMR	1.68 (0.10)	1.82 (0.10)	1.75 (0.11)	1.79 (0.08)
A99SB-V	1.64 (0.08)	**1.91 (0.13)**	1.80 (0.10)	1.75 (0.08)
AMBER-FB15	1.47 (0.07)	1.77 (0.10)	1.75 (0.08)	1.88 (0.10)